Materials Today Bio 25 (2024) 100986

Contents lists available at ScienceDirect

Materials Today Bio

journal homepage: www.journals.elsevier.com/materials-today-bio

Slow and steady wins the race: Fractionated near-infrared treatment empowered by graphene-enhanced 3D scaffolds for precision oncology

Giordano Perini [a,b,1], Valentina Palmieri [b,c,1], Andrea Papait [b,d], Alberto Augello [b], Daniela Fioretti [e], Sandra Iurescia [e], Monica Rinaldi [e], Elsa Vertua [f], Antonietta Silini [f], Riccardo Torelli [g], Angela Carlino [h], Teresa Musarra [i], Maurizio Sanguinetti [g,j], Ornella Parolini [b,d], Marco De Spirito [a,b], Massimiliano Papi [a,b,*]

[a] Dipartimento di Neuroscienze, Università Cattolica del Sacro Cuore, Largo Francesco Vito 1, 00168, Rome, Italy
[b] Fondazione Policlinico Universitario A. Gemelli IRCSS, 00168, Rome, Italy
[c] Istituto dei Sistemi Complessi, CNR, Via dei Taurini 19, 00185, Rome, Italy
[d] Dipartimento di Scienze della Vita e Salute Pubblica, Università Cattolica del Sacro Cuore, 00168, Rome, Italy
[e] Istituto di Farmacologia Traslazionale (IFT), Dipartimento di Scienze Biomediche, CNR, 00133, Rome, Italy
[f] Centro di Ricerca Eugenia Menni, Fondazione Poliambulanza Istituto Ospedaliero, 25124, Brescia, Italy
[g] Dipartimento di Scienze di Laboratorio e Infettivologiche, Fondazione Policlinico Universitario A. Gemelli IRCCS, 00168, Rome, Italy
[h] Dipartimento di Medicina e Chirurgia, Università Internazionale San Camillo per la Salute e le Scienze Mediche (Unicamillus), 00131, Rome, Italy
[i] Unità di Patologia Testa e Collo, Polmone e Endocrinologia, Fondazione Policlinico Universitario Agostino Gemelli IRCCS, 00168, Rome, Italy
[j] Dipartimento di Scienze Biotecnologiche di Base, Cliniche Intensivologiche e Perioperatorie-Sezione di Microbiologia, Università Cattolica del Sacro Cuore, Rome, Italy

ARTICLE INFO

Keywords:
Graphene oxide
3D printed scaffolds
Cancer therapy
Near-infrared radiation
Photodynamic therapy

ABSTRACT

Surgically addressing tumors poses a challenge, requiring a tailored, multidisciplinary approach for each patient based on the unique aspects of their case. Innovative therapeutic regimens combined to reliable reconstructive methods can contribute to an extended patient's life expectancy. This study presents a detailed comparative investigation of near-infrared therapy protocols, examining the impact of non-fractionated and fractionated irradiation regimens on cancer treatment. The therapy is based on the implantation of graphene oxide/poly (lactic-co-glycolic acid) three-dimensional printed scaffolds, exploring their versatile applications in oncology by the examination of pro-inflammatory cytokine secretion, immune response, and in vitro and in vivo tumor therapy. The investigation into cell death patterns (apoptosis vs necrosis) underlines the pivotal role of protocol selection underscores the critical influence of treatment duration on cell fate, establishing a crucial parameter in therapeutic decision-making. In vivo experiments corroborated the profound impact of protocol selection on tumor response. The fractionated regimen emerged as the standout performer, achieving a substantial reduction in tumor size over time, surpassing the efficacy of the non-fractionated approach. Additionally, the fractionated regimen exhibited efficacy also in targeting tumors in proximity but not in direct contact to the scaffolds. Our results address a critical gap in current research, highlighting the absence of a standardized protocol for optimizing the outcome of photodynamic therapy. The findings underscore the importance of personalized treatment strategies in achieving optimal therapeutic efficacy for precision cancer therapy.

1. Introduction

The search for innovative strategies to address the complex nature of cancer has led to significant advancements in the realm of biomaterials and tissue engineering [1,2]. In recent years, significant advancements have been made in scaffold design and fabrication techniques, allowing for precise control over scaffold architecture, composition, and bioactivity [3–5]. Among these advancements, the integration of three-dimensional (3D) printing technology with novel biomaterials has emerged as a cutting-edge approach with immense potential [6–8]. These scaffolds serve as templates to guide tissue regeneration, enabling the formation of functional and organized tissues [9].

* Corresponding author. Dipartimento di Neuroscienze, Università Cattolica del Sacro Cuore, Largo Francesco Vito 1, 00168, Rome, Italy.
E-mail address: massimiliano.papi@unicatt.it (M. Papi).
[1] Authors contributed equally to this work.

https://doi.org/10.1016/j.mtbio.2024.100986
Received 13 November 2023; Received in revised form 25 January 2024; Accepted 29 January 2024
Available online 9 February 2024
2590-0064/© 2024 The Authors. Published by Elsevier Ltd. This is an open access article under the CC BY-NC-ND license (http://creativecommons.org/licenses/by-nc-nd/4.0/).

Graphene oxide (GO), a derivative of graphene, has gathered substantial attention due to its remarkable features and versatile applications in the biomedical field [10–13]. GO is a well-known photosensitizing agent, that can absorb near-infrared (NIR) light and convert it efficiently into heat [14–16]. Moreover, GO demonstrates excellent capability to generate reactive oxygen species (ROS) upon light irradiation, promoting selective destruction of tumor cells while minimizing damage to healthy tissues [17–20]. In combination with biocompatible polymers, such as poly(lactic-co-glycolic acid) (PLGA), GO can be used to create 3D printed scaffolds, offering a powerful platform for both cancer treatment and, at the same time, tissue regeneration [21,22]. PLGA is renowned for its outstanding biocompatibility, making it well-suited for biomedical applications. Its use in scaffold fabrication is particularly advantageous, as PLGA can be easily processed, facilitating the integration of nanomaterials such as GO [23,24]. Furthermore, the selection of PLGA is strategic in the field of scaffolds and prosthetics due to its tunable properties. Indeed, the copolymer composition of PLGA, combining lactic acid (PL) and glycolic acid (GA), allows for precise modulation of mechanical properties by adjusting PL/GA ratio [24]. Increasing the GA content, for instance, enhances the scaffold's strength, while augmenting the PL component improves flexibility. This tunability is crucial for addressing specific clinical needs, such as the type of tissue reconstruction, and accommodating anatomical requirements [23]. Moreover, PLGA provides the added advantage of customizable degradation and resorption kinetics, according to clinical demands [25]. Increasing the percentage of GA in the PLGA composition results in scaffolds that degrade more rapidly. Conversely, adjusting the ratio in favor of PL extends the degradation timeline, providing flexibility in designing scaffolds tailored to different clinical scenarios.

The unique characteristics of GO, including its excellent biocompatibility, high surface area, drug-loading capacity and tunable photothermal/photodynamic properties, make it an ideal candidate for multifunctional therapeutics [26–29]. In recent years, photothermal therapy (PTT) and photodynamic therapy (PDT) have emerged as promising strategies for cancer treatment, harnessing the localized generation of heat and ROS in response to external light irradiation in the presence of photosensitizing agents [30,31]. PDT involves the administration of photosensitizing agents, which, upon exposure to light of a specific wavelength, undergo activation. This activation induces the generation of ROS, resulting in localized damage to cancer cells. Several clinical applications of PDT have demonstrated its efficacy across different malignancies. Dermatological studies showcase PDT as a successful method for treating skin cancers, including basal cell carcinoma and actinic keratosis [32]. The precision of PDT allows for targeted treatment of cancerous lesions while minimizing damage to healthy tissue. In gastrointestinal cancers, particularly esophageal and early-stage gastric cancers, PDT has proven effective. The localized effects of PDT, facilitated by direct light delivery during endoscopic procedures, enhance the treatment precision. Lung cancer, both in early and advanced stages, has been a focus for PDT interventions [33]. PDT for bladder cancer involves intravesical administration of photosensitizing agents directly into the bladder offers a targeted approach for treating superficial tumors [34]. The adaptability of PDT across various cancer types and anatomical locations reflects its potential as a non-invasive and targeted therapeutic approach. As we explore the integration of advanced nanomaterials like graphene or MXenes into PTT/PDT strategies, a new frontier emerges. These nanomaterials exhibit exceptional properties, including high photothermal conversion efficiency. In simpler terms, they efficiently convert IR light, which penetrates tissues deeply, into heat.

To date, optimizing the appropriate NIR radiation dose for PTT/PDT remains largely unexplored, with extremely limited prior research focusing on identifying the most effective and efficient administration of such therapies for anticancer treatment [35,36]. Therefore, in this study, we aim to bridge this critical gap by conducting a comprehensive investigation comparing two distinct strategies: a single radiation session lasting 9 min, non-fractionated (NF) versus a fractionated approach comprising three radiation sessions of 3 min each, administered consecutively over three consecutive days (t1, t2, and t3). We irradiated 3D printed PLGA scaffolds having different concentrations of GO with an infrared laser at different power densities both in vitro and in vivo to provide a comprehensive understanding of the therapeutic outcomes. In the in vitro assessments, we focused on crucial parameters such as cell viability, production of ROS, expression of cytokines, and the type of cell death induced by each PTT/PDT strategy. To evaluate the translational potential of our findings, we established a murine breast cancer model wherein mice were inoculated with cancer cells and subsequently implanted with the PLGA-GO scaffolds. Even after a short-term application of the NIR treatment, noticeable regression of the tumor was observed. We observed distinct variations in the therapeutic responses elicited by the two PTT/PDT strategies. Notably, fractionated (t3) demonstrated a superior efficacy both in vitro and in vivo, suggesting its potential as a more robust approach for anticancer treatment, providing valuable insights into the comparative efficacy of NF and t3 strategies in the context of PTT/PDT.

The results highlight the potential of this approach for targeted cancer cell eradication and reducing immune toxicity. The comparative evaluation of two different doses of NIR radiation provides valuable insights into the efficacy of different treatment protocols and can help to identify the most effective approach for anticancer treatment, paving the way towards clinical translation to the emerging field of PTT/PDT-based therapies.

2. Materials and methods

2.1. GO characterization, 3D printing and characterization of PLGA-GO scaffolds

GO (Graphenea) was characterized by atomic force microscopy (AFM), dynamic light scattering (DLS), Raman spectroscopy, X-ray photoelectron spectroscopy (XPS). Raman spectra of GO were acquired at room temperature using backscattering geometry on an inVia Renishaw micro-Raman spectrometer, which was equipped with an air-cooled CCD detector and super-Notch filters. The excitation source employed was an Ar+ ion laser with a wavelength (λlaser) of 514 nm, coupled to a Leica DLML microscope featuring a 20× objective. The spectral resolution achieved was 2 cm^{-1}, and calibration was performed utilizing the 520.5 cm^{-1} line of a silicon wafer. For XPS, GO was drop-casted on a Si(100) surface. Measurements were conducted utilizing a customized Omicron NanoTechnology MXPS system. The system was outfitted with a monochromatic Al Kα X-ray source (Omicron XM-1000), operating the anode at 14 kV and 16 mA, with a photon energy (hν) of 1486.7 eV. DLS and Zeta potential analysis were conducted using a Zetasizer Nano S from Malvern Instruments, Malvern, UK, equipped with a 4 mW He–Ne laser (633 nm). Measurements were undertaken at a constant angle of 173° relative to the incident beam.

To obtain PLGA-GO composites, PLGA flakes (Rimless Industry) and GO (Graphenea) were mixed keeping a fixed amount of PLGA and varying GO from 0 to 5% w/w in dichloromethan (Carlo Erba). The mixture of PLGA and GO was put in agitation overnight, then air dried. The produced film was cut into small pieces, then it was transferred to a thermoplastic printhead (Cellink), having a heating capacity of up to 250 °C. The structure of scaffolds was designed using modeled 3D computer graphics and computer-aided design (CAD) software Rhinoceros software (Robert McNeel & Associates). PLGA-GO scaffolds were printed via an extrusion-based technique at a printhead temperature of 185 °C and a printbed temperature of 65 °C. The extrusion pressure was set at 40 kPa, with a preflow of 20 ms and a speed of 22 mm/s. GO from Graphenea was characterized by AFM with a NanoWizard II (JPK Instruments). Scaffolds were microscopically characterized through AFM as well. For this purpose, samples were imaged by using silicon

cantilevers with high aspect-ratio conical silicon tips (CSC36 Mikro-Masch) characterized by an end radius of about 10 nm, a half conical angle of 20°, and a spring constant of 0.6 N/m. Small scan areas (3 × 3 μm for GO, 10 × 10 μm for scaffolds) were imaged. Surface roughness parameters were extrapolated for scaffolds with the JPK Data Processing software (JPK Instruments). Scanning electron microscopy (SEM) images were acquired with SEM Supra 25 (Zeiss). All the samples were sputter-coated with gold. Fourier-transform infrared spectroscopy (FTIR) was conducted with an ALPHA II compact FTIR spectrometer (Bruker), to evaluate the correct surface chemical composition of scaffolds. Samples were directly laid upon the crystal and the spectra were recorded in the wave number range of 4000–550 cm^{-1}.

2.2. Near-infrared laser

A NIR laser (LaserEver) focused at 808 nm was used to perform PDT on cells. First, the laser was characterized by evaluating the laser power at every current intensity by using a power meter. The spot of the laser had a diameter of 0.8 cm. The power density was evaluated by normalizing the laser power to the area of the spot. To test the photothermal conversion of PLGA-GO scaffolds, constructs having different concentrations of GO -ranging from 0 to 5% w/w- were used. Scaffolds were put in a 48-well (Corning) and covered with 300 μL of culture medium. Then, they were irradiated at different power densities, depending on the concentration of GO, to achieve the same final temperature. Scaffolds having GO at 0.5% were irradiated with a current of 1.1 A, corresponding to a power density of 0.9 W/cm^2. Scaffolds of PLGA-GO 1% were irradiated with a current of 1.08 A, corresponding to a power density of 0.85 W/cm^2. Scaffolds of PLGA- GO 2% were irradiated with 1.06 A, corresponding to 0.8 W/cm^2. Finally, scaffolds of PLGA-GO 5% were irradiated at 1.02 A, corresponding to 0.75 W/cm^2. Scaffolds without GO were irradiated with the same power density of GO 0.5%, since no thermal increase was observed due to the absence of photoabsorbers. Thermal increase was monitored using a thermal camera (Optris) focused on the well. Two distinct PTT/PDT strategies were used in this work: a single radiation of 9 min (not fractioned, NF) and 3 radiations of 3 min each, one per day (t1, t2 and t3).

2.3. Evaluation of the photodynamic effect

To verify the direct photodynamic conversion effect of the scaffolds, the ROS-ID detection kit (Enzo Life Sciences) was employed. The kit allows for the assessment of comparative levels of total ROS, while also enabling the determination of superoxide production. The kit comprises two major components: the Oxidative Stress Detection Reagent (Green) for ROS detection and the Superoxide Detection Reagent (Orange). The green probe reacts directly with a broad spectrum of reactive species, yielding a green fluorescent product indicative of cellular production of various ROS types. In contrast, the orange probe, a cell-permeable superoxide detection dye, specifically reacts with superoxide, generating an orange fluorescent product. In our study, we irradiated PLGA-GO scaffolds in 48-well plates (Corning) for 3 min or 9 min, to reproduce the experimental conditions of the two NIR regimens. Scaffold were immersed in the Detection Solution during the timecourse of the experiment. After NIR, the 3D-printed constructs were incubated at 37 °C, 5% CO_2 for 1 h. Then, fluorescence intensity in the supernatant was recorded with a Cytation 3 Cell Imaging Multi-Mode Reader (Biotek) by exciting at 490 nm and reading the emission at 525 nm (green probe) and by exciting at 550 nm and reading the emission at 620 nm (orange probe).

2.4. Cell culture

A549 human lung adenocarcinoma cells, 4T1 and 4T1-luc2 mouse mammary and the RAW 264.7 murine macrophage cell line were purchased from the American Type Culture Collection (ATCC; CRL-2539TM, CRL-2539™, CRL-2539-LUC2, TIB-71™). A549 cells were maintained in Dulbecco's modified Eagle's medium DMEM medium-high glucose (D6429, Merck KGaA-Sigma Aldrich, Darmstadt, Germany) supplemented with 10% fetal bovine serum (FBS, GibcoTM 10270106, Thermo Fisher Scientific Inc.), 2 % penicillin-streptomycin (10,000 U/ml, GibcoTM 15140122, Thermo Fisher Scientific Inc.). 4T1 and 4T1 luc2 cells were maintained in RPMI 1640 Medium-ATCC modification) (A1049101, Thermo Fisher Scientific Inc) supplemented with 10 % FBS (GibcoTM 10270106, Thermo Fisher Scientific Inc.), and 2 % penicillin-streptomycin (10,000 U/ml, GibcoTM 15140122, Thermo Fisher Scientific Inc.). 4T1-Luc2 cells are a luciferase-expressing cell line derived from parental line CRL-2539 by transduction with lentiviral vector encoding firefly luciferase gene (luc2). RAW 264.7 cells were maintained in DMEM (D6429, Merck KGaA-Sigma Aldrich, Darmstadt, Germany) supplemented with 10% FBS (GibcoTM 10270106, Thermo Fisher Scientific Inc.), 2 % penicillin-streptomycin (10,000 U/ml, GibcoTM 15140122, Thermo Fisher Scientific Inc.). Cells were kept in T75 flasks (Corning) at 37 °C, 5% CO_2 for further treatments. Human peripheral blood mononuclear cells (PBMCs) were obtained from heparinized whole blood samples using density gradient centrifugation (Histopaque 1077, Sigma-Aldrich).

2.5. Assay protocol to measure viability

WST-1(4-(3-(4-iodophenyl)-2-(4-nitrophenyl)-2H-5-tetrazolio)-1,3-benzene-disulfonate (ROCHE/CELLPRO-RO) colorimetric assay was carried out to determine the effects of NIR laser irradiation (808 nm) on cell proliferation at the above indicated condition. The assay was performed by 48-well plates, with seeding of 4T1 (5×10^3 cells/well), A549 (1×10^4 cells/well), RAW264.7 (3×10^4 cells/well) cells on PLGA, PLGA-GO1% and PLGA-GO2% scaffolds. After each NIR application, cells were cultured for additional 24 h s and 30 μL per well of WST-1 solution were added to the culture medium and incubated for 2 h at 37 °C and 5% CO2. Absorbance was subsequently determined using Cytation 3 Cell Imaging Multi-Mode Reader (Biotek) applying the wavelengths 450 nm for measurements and 650 nm for reference. All experiments were conducted in two wells for each condition and replicated at least three times. Cell proliferation was calculated by comparing the absorbance values of the samples after background subtraction. Cell viability was expressed as the percentage of cells seeded on PLGA. Cell viability of human PBMCs was assessed by staining PBMC harvested from the different culture conditions and by staining cells with E-Fluor 780 (Thermofisher) to exclude dead cells. Stained cells were then acquired at FACS Symphony A3 within 1 h and results analyzed using Flowjo 10.7v (BD Biosciences).

2.6. ROS production

The production of ROS was evaluated to address the photodynamic effect of PLGA-GO scaffolds on cells. For the detection of ROS, the fluorinated derivative of 2′,7′-di-chlorofluorescein (H_2DCFDA) was employed. This probe is nonfluorescent until the acetate groups are removed by intracellular esterases and oxidation occurs within cells. Thus, oxidation can be detected by monitoring the increase in the fluorescence intensity. Cells were seeded on 48-well plates (Corning), having PLGA-GO scaffolds on the bottom of each well, at a seeding density of 3×10^5 cells/well. Plates were then incubated at 37 °C, 5% CO_2. After incubation, scaffolds having different concentrations of GO, ranging from 0 to 5% w/w were irradiated with an 808 nm infrared laser at different power densities to induce the same thermal increase. The two different therapeutic approaches previously described were used: NF and t3. After the treatment, the medium was replaced with PBS containing 10 μM H_2DCFDA. Cells were incubated for 30 min at 37 °C in 5 % CO_2. PBS containing H_2DCFDA was then removed, and cells were resuspended in complete medium. The fluorescence intensity of H_2DCFDA was recorded by using a Cytation 3 Cell Imaging Multi-Mode

Reader using an excitation wavelength of 495 nm and recording the emission at 528 nm. To correctly quantify the production of ROS after the treatment, results were normalized by the number of viable cells and expressed as folds change with respect to cells seeded on PLGA.

2.7. ELISA assay on cells supernatant

RAW264.7, 4T1 and A549 cell lines were seeded on PLGA, PLGA-GO 1% and PLGA-GO 2% scaffold in a 48-well plate at 3×10^4, 5×10^3 and 1×10^4 cells/well, respectively. NIR laser irradiation (808 nm) was conducted on cell proliferation at the above indicated condition and supernatants were collected after each NIR application centrifuged at 1200 rpm for 5 min and stored at −80 °C until use. Tumor necrosis factor-α (TNF-α), interleukin-6 (IL-6) and interleukin-8 (IL-8) release was measured in 4T1 and A549 culture medium using mouse or human ELISA development kits (PeproTech® EC Ltd., UK), respectively, according to the manufacturer's instructions. For mouse IL-8 detection was used macrophage inflammatory protein-2 (MIP-2) ELISA kit as it is the mouse functional IL-8 homologue. RAW264.7 supernatants were tested for mouse TNF-α (MABTECH, Sweden) IL-6 (Invitrogen, MA, USA), and IL-1β (MyBioSource Inc., San Diego, CA). Supernatants were diluted 1:2 and recombinant standards were serially diluted according to the manufacturers' instructions in diluent solution and added to 96-well plates. Interleukins binding were detected by chromogen 2,2′-azino-bis (3-ethylbenzothiazoline-6-sulphonic acid (ABTS) or 3,3′,5,5′-Tetramethylbenzidine (TMB) incubation, and color development was monitored at 405 nm or 450 nm, respectively, according to the manufacturers' instructions. The concentration of cytokines in the samples was determined from the standard curve.

2.8. ELISA assay on mouse serum

Sera diluted 1:2 were used for the detection of interleukin-6 (IL-6), tumor necrosis factor-α (TNF-α), and macrophage inflammatory protein 2 (MIP-2) using mouse ELISA development kits (PeproTech® EC Ltd., UK) according to the manufacturer's instructions as already described above. Interleukins binding were detected by chromogen 2,2′-azino-bis (3-ethylbenzothiazoline-6-sulphonic acid (ABTS) and color development was monitored at 405 nm.

2.9. Pattern of cell death assessed by WST-1 assay after NIR treatment

4T1 and A549 cells (5×10^3 and 1×10^4 cells/well) were seeded on PLGA-GO 2% scaffold and cultured in a 48-well plate. After 24 h, Caspase- or RIPK1-inhibitors (Z-VAD-FMK, Promega WI, USA; RIP1 inhibitor II, 7-Cl-O-Nec-1, Calbiochem, Merck KGaA Darmstadt, Germany) were added into the wells at final concentrations of 20 μM, or PBS as control, and NIR laser irradiation were conducted after 1 h. Each inhibitor was added to cancer cells before each NIR irradiation (three times in the t3 regimen and once in the NF regimen). The culture medium was refreshed each day during the t3 experiment, and the inhibitor was newly added to restore the required 20 μM concentration. 24 hrs after NIR irradiation, the WST-1 reagent was added for another 2 h and the resulting amount of formazan dye was analyzed by spectrophotometry at 450 nm.

2.10. In vivo antitumor therapy and tumor evaluation

All animal care and experimentation were conducted in compliance with the guidelines of the European Union Directive 2010/63 and the Italian Law D.Lgs. 26/2014 and with the approval of the Institutional Animal Experimentation Ethics Committee of 'Università Cattolica del Sacro Cuore (Rome, Italy) and the Italian Health Ministry registered under No. 223/2022-PR. Animal studies are reported in compliance with the ARRIVE guidelines. All possible efforts were made to minimize animal suffering and to reduce the number of animals used per condition by calculating the necessary sample size before performing the experiments.

The animals were maintained at 22 ± 2 °C under a 12 h–12 h light/dark cycle with 50–60% humidity for at least one week prior to the experiment.

Eight/nine-week-old female BALB/c mice, weighing 19,13 ± 0,93 g were subcutaneously injected into the backs with 50 μl of 4T1-luc2 cells suspension (2×10^6 cells/ml) to establish the ectopic breast cancer model. 4T1-Luc2 cells express luciferase through lentiviral vector encoding firefly luciferase gene (luc2) under control of EF-1 alpha promoter.

One week post tumor challenge, four groups were randomly established (n = 4): Tumor group (T), without adding any scaffolds or NIR, Tumor and Scaffold group (TS), tumor, scaffold and the Not Fractioned single NIR radiation treatment (NF), tumor, scaffold and the fractioned t1, t2, t3 (t3).

Animals were fully anesthetized by intraperitoneal injection 10 ml/kg of a solution composed by ketamine hydrochloride (8 mg/ml, Ketavet 100, MSD Animal Health S.r.l., Italy) and xylazine (0.7 mg/ml, Rompun 20, Bayer S.p.A., Germany). Buprenorphine (0.1 mg/kg, diluted to 0.015 mg/ml) was administered subcutaneously prior to recovery from anesthesia.

A small skin incision was carefully made at the edge of the tumor and the scaffolds were implanted beneath the tumor tissues. The skin was sutured with 6-0 suture string (Assut Europe, Italy) and groups NF and t3 were exposed, still under anesthesia, to the NIR laser at 0.8 W/cm^2 for 9 min or 3 min respectively, and the temperatures of tumor surface were recorded by a thermal camera (Optris) in real time during the treatment. Group t3 received the 3 min irradiation the next two days, also, under isoflurane anesthesia (2% isoflurane).

Tumor bioluminescence was evaluated to monitor tumor growth by Optical Imaging IVIS® System every 7 days starting from NIR treatment, named day 0, while animals were under isoflurane anesthesia. Images were acquired 10 min after intraperitoneal injection of D-luciferin (25 mg/ml - 150 mg/kg). The first NIR treatment day was regarded as day 0. From day −7, mice weight was measured at each time point to verify animal health conditions.

Mice were sacrificed by cervical dislocation under general anesthesia 2 weeks after day 0, tumor tissues were soaked in 4% neutral buffered formalin, embedded in paraffin, sectioned into slices and stained with hematoxylin-eosin (H&E) in sequence and finally evaluated under light microscopy (Leica). Five tissue slices were selected from each sample, and then five visions were measured from each slice randomly. Blood samples were collected postmortem by cardiac puncture and, after 15–30 min at room temperature, centrifuged at 1000–2000×*g* for 10 min in a refrigerated centrifuge. The resulting sera were transferred into a clean polypropylene and stored at −80 °C.

2.11. Analysis of PBMC proliferation

The collection of human peripheral blood mononuclear cells (PBMC) from healthy donors for research purposes was approved by the local ethical committee "Comitato Etico Provinciale di Brescia," Italy (NP 3968, July 2, 2020). PBMCs (1×10^5/well in a 96-well plate) were activated with 125 ng/mL (final concentration) of anti-CD3 monoclonal antibody (Orthoclone OKT3, Janssen-Cilag, Cologno Monzese, Italy). Activated PBMCs (PBMC + anti-CD3) were grown for 3 days in RPMI 1640 medium (Cambrex) supplemented with 10% heat-inactivated FBS, 2 mM L-glutamine and P/S in the presence of PLGA scaffold or a scaffold of PLGA-GO at different concentrations (0.5, 1, 2, 5%), exposed or not to two different regimens of hypothermia induced by either NF or t3 with infrared laser. Activated PBMCs stimulated with infrared laser regimens in absence of scaffolds were used as controls in all experiments. All conditions were performed in triplicate. PBMC proliferation was assessed by incorporation of 5-ethynyl-2′-deoxyuridine (EdU) as previously described. Briefly, 10 μM EdU (Life Technologies) was added to

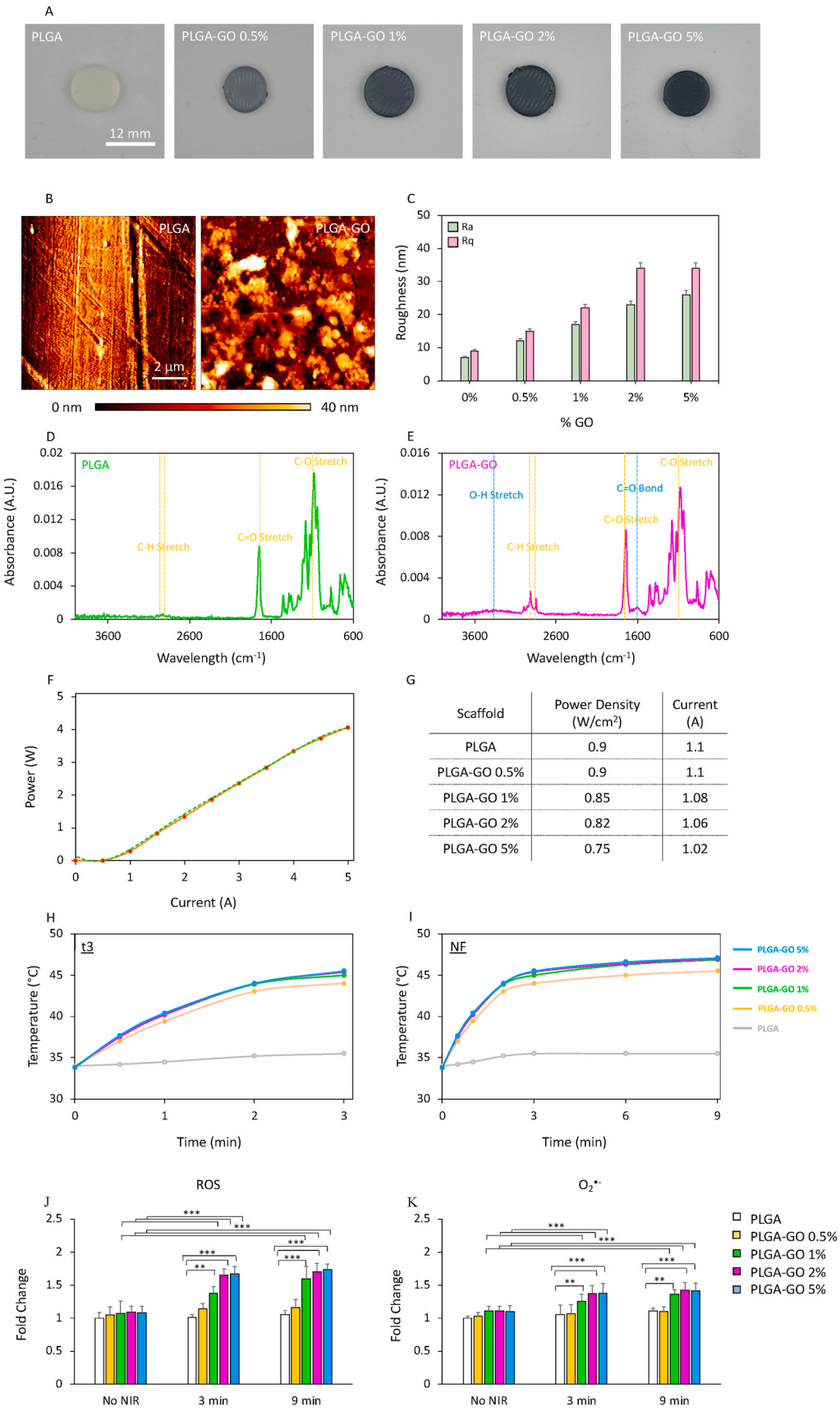

Fig. 1. Characterization of PLGA-GO scaffolds. **A**) Pictures of 3D printed PLGA-GO scaffolds having different concentrations of GO. **B**) AFM representative images of PLGA and PLGA-GO 2% scaffolds. **C**) Surface roughness of 3D printed scaffolds. **D-E**) FTIR spectra of PLGA and PLGA-GO scaffolds. **F**) Characterization of the 808 nm laser. **G**) NIR radiation specifications for the 3D printed materials. **H-I**) Temperature increase in a timespan of 3 min (t3) and 9 min (NF) for PLGA-GO scaffolds. **J-K**) Production of ROS induced by irradiating scaffolds without cells for 3 or 9 min $^{**}p > 0.01$ and $^{***}p > 0.001$ ANOVA and Turkey post-hoc test.

PBMCs at day 3 post-stimulation. After 16–18 h, cells were harvested and EdU incorporation was assessed by adding 2.5 μM 3-azido-7-hydroxycoumarin (Jena Biosciences) in a buffer solution (100 mM Tris-HCl pH 8.0, 10 mM L-ascorbic acid, 2 mM $CuSO_4$) at RT for 30 min. Cells were acquired with a FACS Symphony A3 (BD Biosciences), and the percentage of EdU-positive proliferating cells was analyzed with Flowjo v10.7. Cells were also stained with E-Fluor 780 (Thermofisher) to exclude dead cells.

2.12. Phenotype of $CD4^+$ T helper (Th) and T regulatory (Treg) subsets

T helper (Th1, Th2, and Th17) and Treg subpopulations were identified by flow cytometry analysis for the expression of specific cell surface markers and transcription factors. After being co-cultured for 5 days with or without PLGA scaffold alone or with GO (0.5, 1, 2, 5%), activated PBMCs were harvested and centrifuged at 300 g for 5 min. The viable dye E-Fluor 780 from Thermofisher was used to eliminate dead cells. CD3 (clone UCHT1), CD4 (clone VIT-4), CD45RA (clone HI100), CD196 (clone 11A9), CD183 (clone 1C6/CXCR3), CD25 (clone M-A25) all purchased from BD biosciences and CD194 (clone REA279) from Miltenyi. After fixation and permeabilization with BD Cytofix/Cytoperm (BD Biosciences), intracellular staining for the transcription factor FoxP3 was carried out by incubating cells with anti-FoxP3 antibody (clone R16-715, BD Biosciences) 4 °C for 30 min in the dark. FACS Symphony A3 (BD Biosciences) was used to acquire the samples, and Flowjo 10.7v (BD Biosciences) was used to analyze the results. Th subsets and Treg were identified by the following gating strategy: first, $CD4^+$CD45RA negative cells were gated to identify T effector cells, then Th subsets were identified as follows: Th1 as CD196-CD183+, Th17/Th1 as CD196+CD183+, Th2 as CD196-CD183-CD194+, and Treg as CD25hiFoxP3+ [37].

2.13. Analysis of monocyte differentiation toward antigen-presenting cells

To induce dendritic cell (DC) differentiation, 2.5 × 105 PBMC were cultured in 48-well plates for four days (Corning) in the presence of 50 ng/mL recombinant human IL-4 (R&D Systems, Minneapolis, MN, USA) and 50 ng/mL granulocyte macrophage colony stimulating (GM-CSF, Miltenyi Biotec) in 0.5 mL RPMI 1640 complete medium (Sigma Aldrich). Complete maturation was reached by adding 0.1 μg/mL lipopolysaccharide (LPS, Sigma Aldrich) for two days.

Monocyte-derived M1 macrophages were obtained from 5×10^5 PBMCs cultured in 24-well plates for four days (Corning) in the presence of 5 ng/mL GM-CSF (Miltenyi Biotec) in 0.5 mL of RPMI 1640 complete medium (Sigma Aldrich). Cells were fully differentiated to M1 macrophages by exogenously administering 20 ng/mL interferon gamma (IFN-γ) for 1 h, followed by 0.1 μg/mL LPS (Sigma-Aldrich) and incubated for two days.

M1 differentiation was assessed by flow cytometry analysis. Cells were stained with E-Fluor 780 (Thermofisher) to exclude dead cells and only live cells were analyzed. The gating strategy is the following: live cells gated as negative for CD3 expression were subsequently analyzed for the expression of CD11b (clone ICRF44). CD11b positive cells were then examined for the expression of CD163 (clone GHI/61), CD209 (clone DCN46), CD197 (clone 3D12), CD86 (clone 2331(FUN-1)), and CD14 (clone MP9) (all antibodies were purchased from BD Biosciences).

2.14. Statistical analysis

For tests on PBMC, the data are represented as violin truncated plots with Tukey variations. The parameters were compared using two-way analysis of variance (ANOVA). Data are representative of at least three independent experiments. Statistical analysis was performed using Prism 8 (GraphPad Software). For all tests on cancer cell lines, one-way ANOVA and Turkey post-hoc test was used. A p value lower than 0.05 was considered statistically significant.

3. Results and discussion

3.1. Characterization of PLGA-GO scaffolds

PLGA-GO scaffolds were 3D printed via an extrusion-based and characterized by atomic force microscopy (AFM) to inspect surface topology and roughness, and by Fourier-transform infrared spectroscopy (FTIR) to confirm the chemical composition of the materials. Results are reported in Fig. 1. Scaffolds with a diameter of 12 mm were 3D printed having different concentrations of GO: 0, 0.5, 1, 2 and 5% w/w (Fig. 1A). AFM imaging depicted a sharply different surface topology between PLGA and PLGA-GO scaffolds (Fig. 1B), highlighting a GO concentration-dependent increase in the surface roughness both in terms of arithmetic average of profile height deviations from the mean line, Ra, and root mean square average of profile height deviations from the mean line, Rq (Fig. 1C). FTIR analysis is reported on Fig. 1D for PLGA and **E** for PLGA-GO scaffolds. Both spectra showed typical absorption peaks at 2990 and 2890 cm^{-1}, corresponding to the C–H stretch of CH_2, and of –C–H– respectively [38]. Moreover, both scaffolds had a peak at 1700 cm^{-1} and a peak at 1000 cm^{-1}, corresponding to the C=O stretching of the ester bond and to the C–O respectively [39]. Interestingly, the presence of GO within the 3D printed materials was confirmed on PLGA-GO spectra by highlighting a broad absorption peak ranging from 3600 to 3100 cm^{-1}, which corresponds to the O–H stretching vibration, and a narrower peak at 1500 cm^{-1}, corresponding to the C=O bond [40,41]. After microscopic and spectroscopic characterization, PLGA-GO scaffolds were tested to perform PTT/PDT. For this purpose, scaffolds were placed on a 48-well plate and immersed in culture medium. 3D printed materials were then irradiated with an 808 nm infrared laser at different power densities, to achieve the same thermal increase regardless the concentration of GO. The laser was first characterized by recording its power with respect to the current (Fig. 1F). NIR radiation was exerted investigating the most effective and efficient approach for administering photothermal/photodynamic radiation as an anticancer therapy. In this study, we compared two distinct photothermal strategies: a single radiation lasting 9 min, namely NF, and a fractionated approach comprising three radiations of 3 min each, administered consecutively over three days (namely t1, t2 and t3). Power densities used for NIR radiation on each scaffold are reported in Fig. 1G. 3D printed PLGA was irradiated with the highest tested power density, expecting no thermal increase over time due to the absence of photoabsorbers within the scaffold. Temperature increase was monitored for both t3 and NF (Fig. 1H and I respectively). All scaffolds reached the same temperature in both timespans, regardless the different concentrations of GO. PLGA scaffolds without GO did not achieve a significant temperature raise in both therapeutic strategies. We then investigated the NIR radiation photodynamic effect on bare scaffolds. Our findings reveal a statistically significant increase in the production of reactive oxygen species (ROS, Fig. 1J) and superoxide ($O_2^{\bullet-}$, Fig. 1K) following scaffold irradiation. Notably, the discrimination between general ROS and superoxide was achieved through the use of two distinct probes: a green fluorescent dye for the detection of general ROS, such as hydrogen peroxide (H_2O_2), peroxynitrite ($ONOO^-$), hydroxyl radicals ($OH^\bullet$), nitric oxide (NO), and peroxy radical (ROO); an orange fluorescent probe, capable of detecting $O_2^{\bullet-}$. This emphasizes the critical importance of evaluating the PDT potential of such constructs, shedding light on their ability to selectively generate ROS and superoxide upon NIR stimulation. The observed rise in ROS production underscores the efficacy of the designed scaffolds in utilizing light energy for therapeutic applications, underscoring their promise in advancing photothermal and photodynamic treatments.

3.2. Comparison of NF/t3 NIR radiation regimens on PBMC viability

Before investigating the effect of hyperthermia on the immune cell functions, we determined whether the exposure to t3 vs NF irradiation

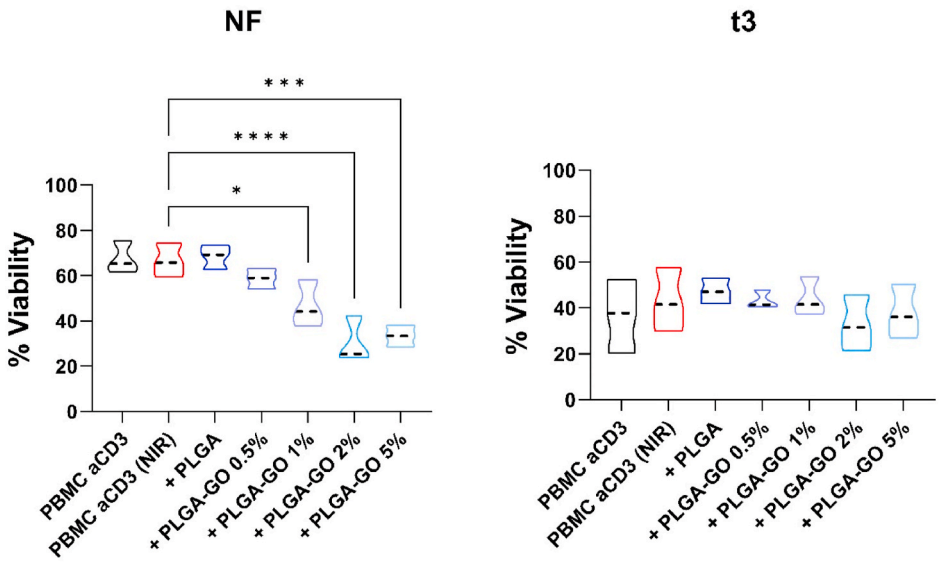

Fig. 2. Impact of hyperthermia regimens on PBMC viability. PBMC were stimulated with anti-CD3 mAb in the presence of PLGA scaffolds conjugated with different concentrations of GO (0.5, 1, 2 and 5%) in comparison to the control condition in red, second lane, at the two different hyperthermia regimens: NF (**A**, left panel) or t3 (**B**, right panel). Results are expressed as percentage of viable cells. Results are displayed as violin plots showing median (thick line), 25th and 75th quartiles (*p < 0.01, ***p < 0.001 versus control (PBMC + anti-CD3), N ≥ 3individual experiments.

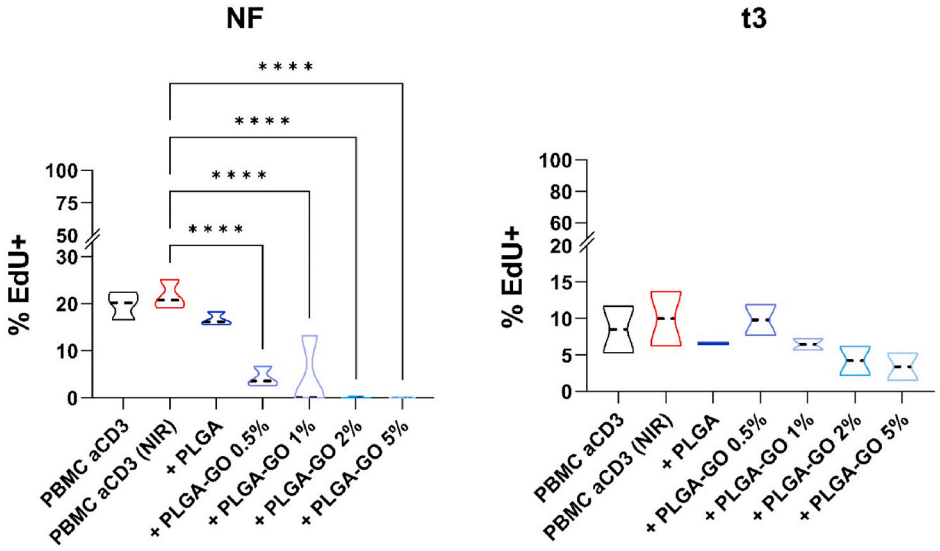

Fig. 3. Impact of hyperthermia regimens on PBMC proliferation. PBMC were stimulated with anti-CD3 mAb in the presence of PLGA scaffolds with different concentrations of GO (0.5, 1, 2 and 5%) in comparison to the control condition in red, second lane, at the two different hyperthermia regimens: NF (**A**, left panel) or t3 (**B**, right panel). Results are expressed as percentage of Edu positive proliferating cells. Results are displayed as violin plots showing median (thick line), 25th and 75th quartiles (*p < 0.01, ***p < 0.001 versus control (PBMC + anti-CD3), A: N ≥ 3; individual experiments.

by infrared laser differently affected the viability of activated PBMC in the different culture conditions (i.e. in presence/absence of PLGA or PLGA-GO scaffolds). We observed that the laser irradiation applied by the NF protocol induces a strong and progressive cell death; this is also observed in the presence of scaffolds with increasing concentrations of GO. A general reduction in cell viability was observed during the t3 treatment. This effect can be attributed to the experimental conditions, which require daily treatment, for three consecutive days. However, laser irradiation of the t3 protocol had minimal effect on cell viability, even at the highest GO concentrations (Fig. 2B, right panel).

3.3. Comparison of NF/t3 NIR radiation regimens on PBMC proliferation

We next sought to assess the impact of irradiation on PBMC proliferation in response to stimulation with anti-CD3 mAb. At first, we found that regardless the protocol applied, irradiation did not affect the ability to PBMC to proliferate in response to anti-CD3 stimuli (violin plot red, second lane for both, Fig. 2A–B). Similarly, the presence of PLGA scaffold did not affect the proliferation of activated PBMC. In contrast, in presence of PLGA-GO scaffolds the application of NF irradiation strongly impaired PBMC proliferation even at the lowest concentration of GO; indeed 1, 2% and 5% PLGA-GO completely inhibited the proliferation of PBMC (Fig. 3A, left panel).

On the other hand, we observed that stimulated PBMC respond better to the stress induced by the hyperthermia when applied as t3 protocol, indeed PBMC proliferation was only slightly reduced in presence of PLGA scaffolds having GO at 0.5% and 1%. The higher GO concentrations, 2% and 5%, induced a reduction in PBMC proliferation but

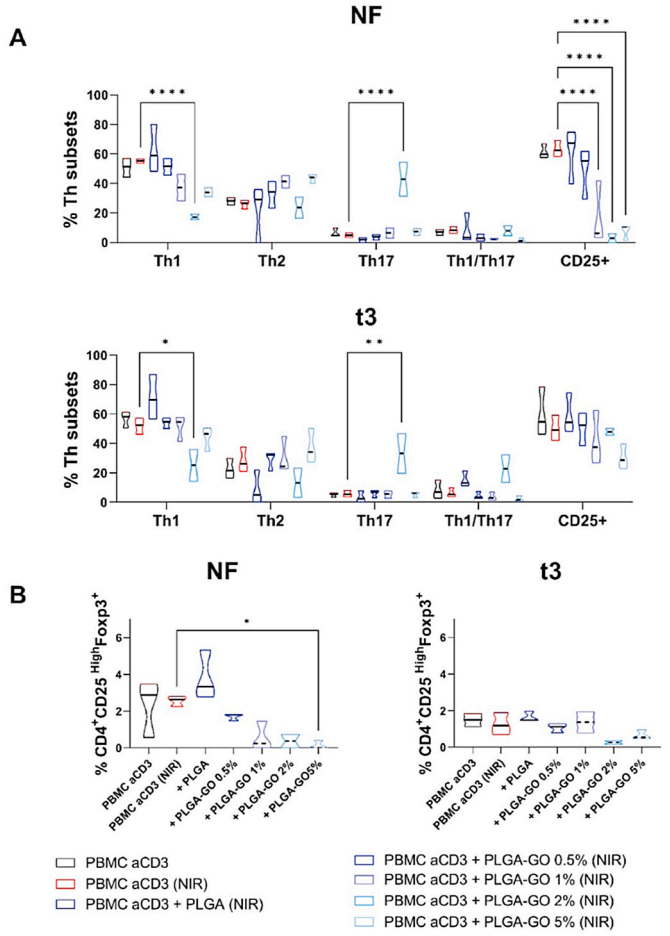

Fig. 4. Impact of hyperthermia regimens on Th subset differentiation and Treg polarization. PBMC were stimulated with anti-CD3 mAb in the presence of PLGA scaffolds at different concentrations of GO (0.5, 1, 2 and 5%) in comparison to the control condition in red, second lane, at the two different hyperthermia regimens: NF (left panel) or t3 (right panel). **A**) Th1 (CD183+CD196−), Th1/Th17 (CD183+CD196+) and Th2 (CD183-CD196-CD194+), Th1/Th17 (CD183+CD196+) and Th17 (CD183-CD196+) phenotypes were evaluated. Furthermore, the expression of the T lymphocyte activation marker CD25 was assessed. **B**) Induction of Treg was evaluated by flow cytometry after six days and displayed as a percentage of CD45RA–FoxP3+CD25hi cells. Results are represented as violin plots showing median (thick line), 25th and 75th quartiles (*p < 0.05, **p < 0.01, ****p < 0.0001 versus control PBMC + antiCD3), N ≥ 3 individual experiments.

without reaching the complete suppression as observed with the NF protocol (Fig. 3B, right panel).

3.4. *Effect of NIR radiation regimens in the differentiation of CD4$^+$ T lymphocytes in different subsets*

We investigated whether different hyperthermia protocols could impact CD4 lymphocyte differentiation in different Th subsets. Again, we observed that hyperthermia/irradiation does not affect the differentiation of both activated PBMCs and of activated PBMC cultured in presence of PLGA scaffolds, confirming the results previously reported for proliferation. Differences were instead observed after the application of the two hyperthermia regimens to activated PBMC in presence of PLGA-GO scaffolds. Again, we observed that NF irradiation strongly affects CD4$^+$ lymphocyte differentiation. In fact, we noted that even 1% GO reduced differentiation toward the inflammatory Th1 subset. At increasing graphene concentrations, we detected a progressive impairment of T lymphocytes ability to differentiate toward Th1 subset

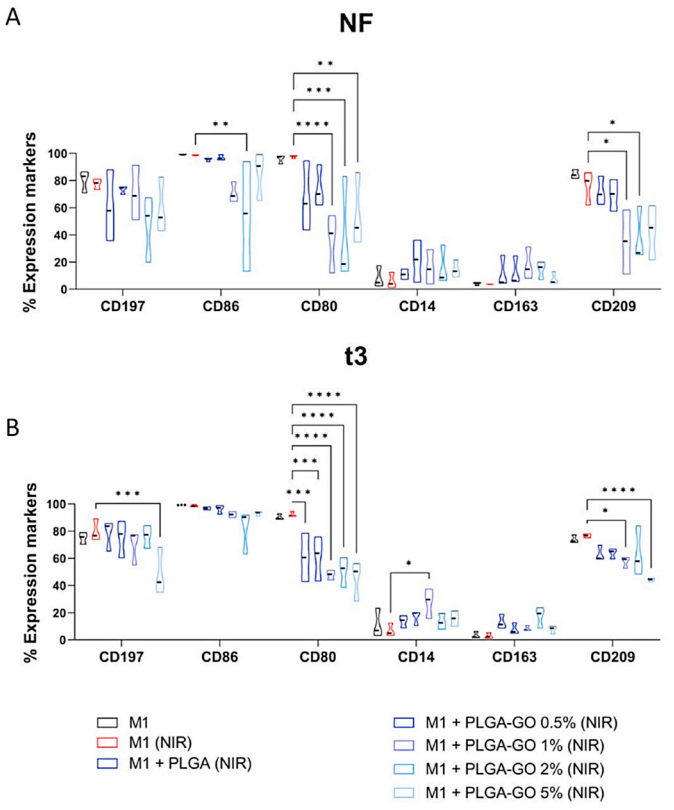

Fig. 5. Comparison of NF and t3 hyperthermia regimen on Monocyte to M1 macrophage differentiation. Phenotype analysis of PBMC differentiated into M1 macrophages in the presence of PLGA scaffolds at different concentration of GO (0.5, 1, 2 and 5%) in comparison to the control condition in red, second lane, represented by fully differentiated M1 macrophages treated with the same hyperthermia regimen, at the two different hyperthermia regimens: NF (**A**, upper panel) or t3 (**B**, lower panel). Scaffolds were added at the start of the differentiation protocol to evaluate the ability to affect monocyte differentiation toward M1 macrophages. At the end of the culture period, expression of CD14, CD209, CD197 and CD163 and of the co-stimulatory molecule CD80 and CD86 was evaluated by flow cytometry. Results are presented as a percentage of expression and are shown violin plots show median (thick line), 25th and 75th quartiles (*p < 0.05, ***p < 0.001, ****p < 0.0001 versus control M1), N ≥ 3 individual experiments.

(Fig. 4A, upper panel), which could be a consequence of reduced cell viability (Fig. 2).

A similar impairment in differentiation efficiency was observed also in the t3 protocol with 1% GO (Fig. 4A, lower panel). Both hyperthermia protocols did not significantly affect CD4 lymphocyte differentiation to Th2, while they significantly increased their polarization toward Th1/Th17 and Th17 in presence of PLGA-GO 2% scaffolds. Finally, we analyzed the expression of the T lymphocyte activation marker CD25. NF treatment heavily affected the expression of this marker similar to the effect previously observed for PBMC proliferation (Fig. 3A). In fact, 1% GO induced a strong reduction of CD25 expression, while the t3 protocol induced a slight reduction of CD25 expression (Fig. 4A).

Finally, we observed that both NF and t3 hyperthermia protocols reduced the polarization toward regulatory T cell subsets, but to a different extent. The NF regimen strongly decreased Treg polarization starting from 0.5% GO, while t3 protocol decreased Treg polarization when 2% GO was Other instead have shown that near-infrared (NIR) radiation, irrespective of its thermal effects, enhances the activation of both T helper (Th) 1 and Th2 immune responses, while it had no impact on regulatory T lymphocytes [42]. It is worth noting that these conflicting observations may arise from differences in experimental conditions, cell types, or specific parameters of photobiomodulation used in

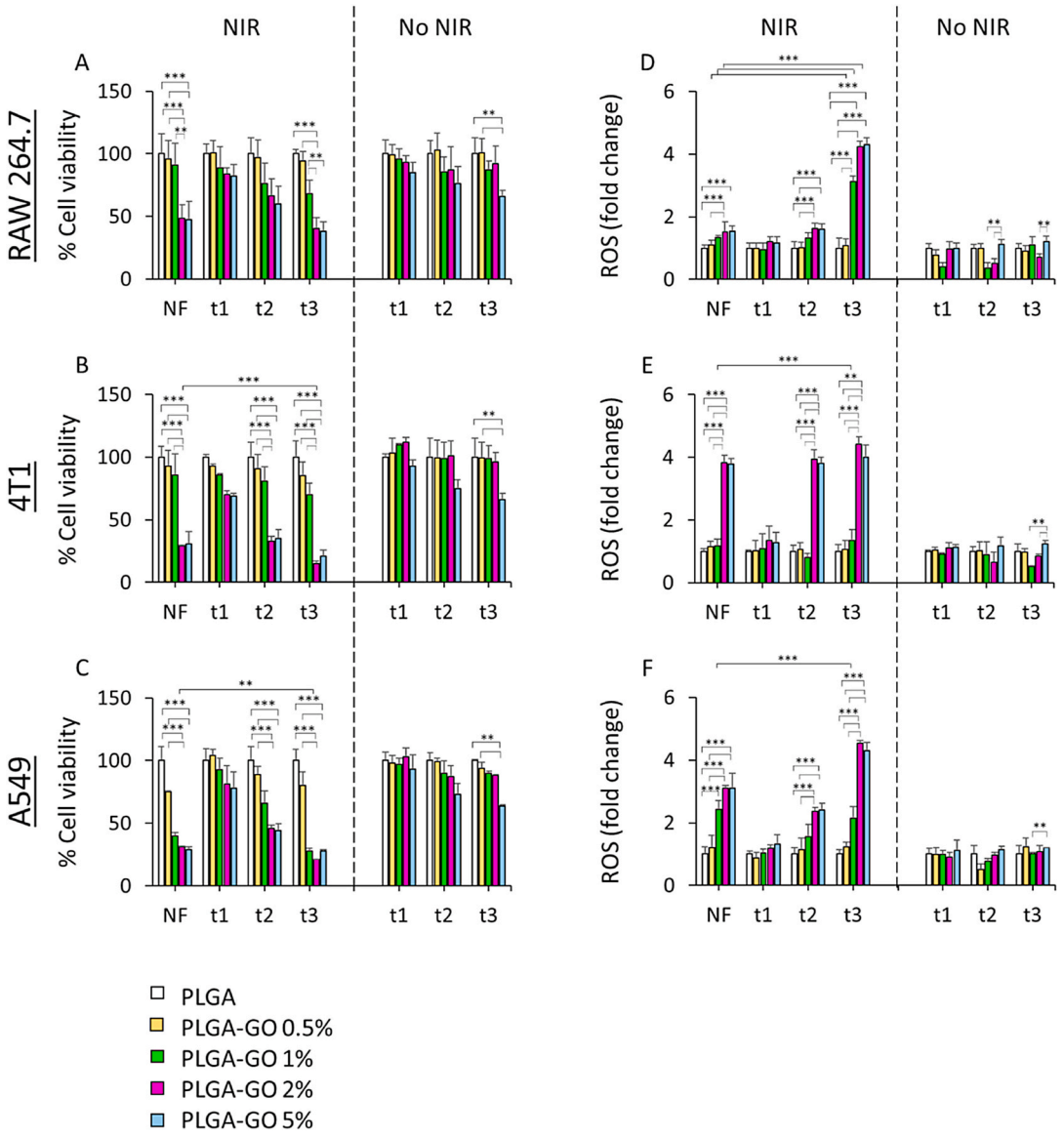

Fig. 6. Biological effect of photothermal/photodynamic treatments (NF and t3) on cells seeded on 3D printed PLGA-GO scaffolds. **A-C**) Cell viability on mouse macrophages, breast cancer cells and human lung adenocarcinoma cells respectively. **D-F**) Photodynamic-induced production of ROS after NF and t3 on mouse macrophages, murine breast cancer cells and human lung adenocarcinoma cells respectively. Results of cell viability are reported as % of cells seeded on LGA. Production of ROS are reported as fold change with respect to cells seeded on PLGA. **p > 0.01 and ***p > 0.001 ANOVA and Turkey post-hoc test.

the respective studies.

3.5. Comparison of NIR radiation regimens in the differentiation of monocyte toward M1 inflammatory macrophages

The differentiation process from monocyte to macrophage occurs, as indicated by the loss of expression of CD14, a monocytes marker, regardless of GO concentration and protocol used (Fig. 5A). On the other hand, however, both hyperthermia protocols significantly reduced the expression of the differentiation marker CD209 as well as the co-stimulatory molecule CD80 in presence of the higher GO concentrations (5, 2 and 1%) (Fig. 5A and B). These findings align with another study that demonstrated that high-intensity infrared photobiomodulation (PBM) doses reduce markers associated with M1 and M2a macrophage phenotypes in vitro and increase the expression of TGFβ1 in M2 macrophages [43]. These results have also been corroborated by in vivo studies, which showed that PBM can reduce TNF-α expression in macrophages activated with LPS + IFN-γ.

3.6. Cell viability and ROS production

The two different NIR radiation protocols were then tested on different cell lines: A549 human lung adenocarcinoma cells, 4T1 mouse triple-negative mammary and RAW 264.7 mouse macrophage cell line.

Cells were cultured on PLGA-GO scaffolds to evaluate antitumor efficacy of the two distinct PTT/PDT regimens, NF and t3. NIR radiation was exerted on PLGA-GO scaffolds having GO at 0%, 0.5%, 1%, 2% and 5% w/w. In vitro evaluation of the two therapeutic strategies was first performed by comparing cell toxicity and production of ROS. Mouse macrophages seeded on PLGA-GO 2% and 5% scaffolds showed a significant decrease in cell viability after both NF and t3 with respect to irradiated PLGA and PLGA-GO 0.5%, while no significant differences were observed between the two therapeutic strategies in terms of viability (Fig. 6A). The two tested cancer cell lines depicted an evident decrease in cell viability after NIR radiation. Particularly, breast cancer cell lineage showed a significantly higher photothermal effect when seeded on PLGA-GO 2% and 5% scaffolds either on NF and on t3

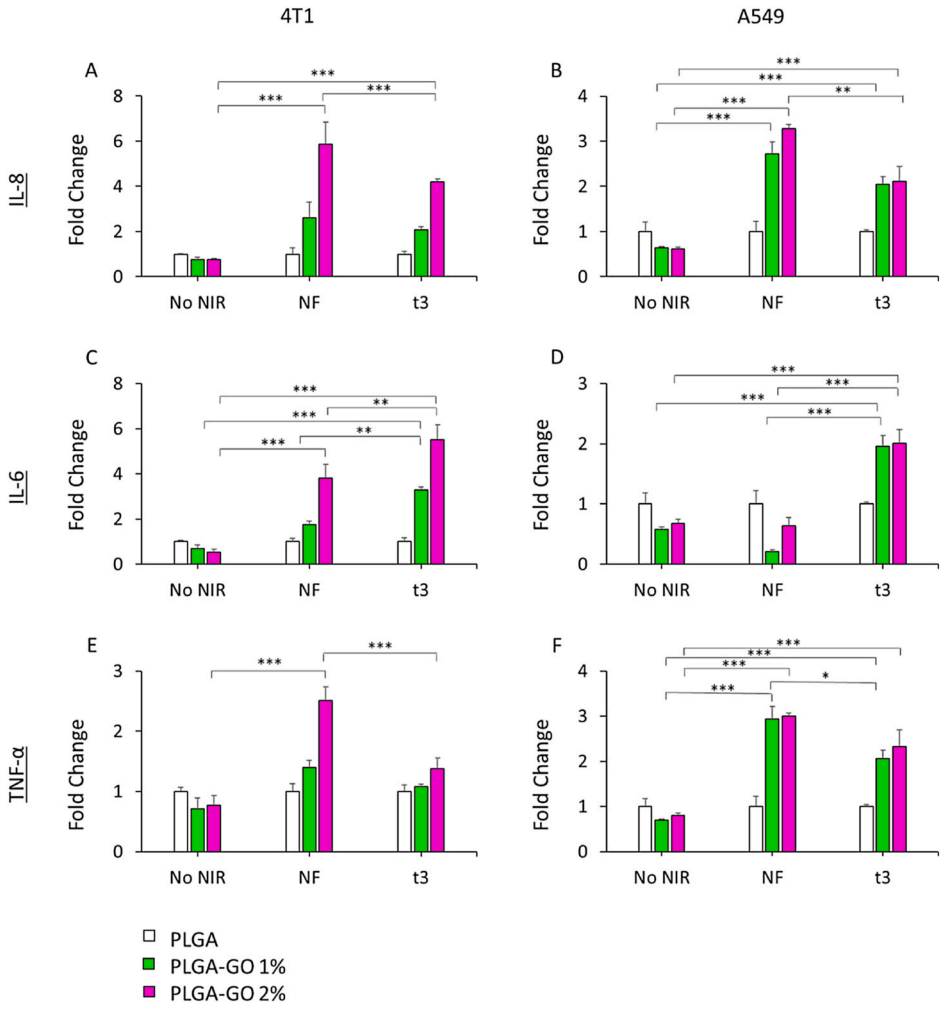

Fig. 7. Expression of cytokines on A459 and 4T1 cancer cell lines. **A**, **B**) Expression of IL-8 on mouse mammary tumor and on human lung adenocarcinoma respectively. **C**, **D**) Expression of IL-6 on mouse mammary tumor and on human lung adenocarcinoma respectively. **E**, **F**) Expression of TNF-α on mouse mammary tumor and on human lung adenocarcinoma respectively. Data are reported as fold change with respect to cells seeded on PLGA. **p > 0.01 and ***p > 0.001 ANOVA and Turkey post-hoc test.

(Fig. 6B). Importantly, t2 also caused a significant reduction in viability on the same samples with respect to irradiated PLGA and PLGA-GO 0.5%. Furthermore, we observed a slight difference between the two NIR therapies. The fractioned t3 radiation caused a significantly higher cell death on PLGA-GO 2% when compared to NF indeed, but not with PLGA-GO 5%. Human lung cancer cell lineage displayed a similar behavior (Fig. 6C). In this case, however, even cells seeded on PLGA-GO 1% had a strong reduction in cell viability after t3 and NF. The therapeutic strategy t3 showed a greater effect on PLGA-GO 1%, 2% and 5% samples with respect to NF. Importantly, for all tested cell lines, a significant reduction in cell viability was observed after seeding on PLGA-GO 5% without the need to perform NIR radiation, indicating an intrinsic toxicity effect probably due to the high concentration of GO. Taken together, these findings point out the different outcomes of two diverse therapeutic approaches based on NIR dose, showing a significantly greater effect on cancer cells after three radiations at the same temperature with respect to a single, longer NF administration. Moreover, the presence of GO in the scaffold holds potential for a specific PDT approach. When GO is exposed to NIR light, it undergoes a nonradiative relaxation process, transferring the absorbed energy to nearby oxygen molecules and generating singlet oxygen species through a type II photochemical pathway. The produced free radicals might exert potent cytotoxic effects by oxidizing biomolecules within the immediate vicinity of GO, leading to cellular damage and eventual cell death. This photodynamic effect of GO under NIR radiation holds immense potential for selective and precise cancer treatment, as it enables the generation of cytotoxic ROS exclusively within the targeted tumor regions while sparing the surrounding healthy tissues. For this reason, we investigated the production of ROS after the two different NIR radiation approaches. Mouse macrophages seeded on PLGA-GO 1%, 2% and 5% scaffolds showed a greater production of ROS when compared to NF therapy (Fig. 6D). Breast cancer cells showed a slightly higher production of ROS after NF, t2 and t3 only on samples seeded on PLGA-GO 2% and 5%. The effect at t3 was significantly greater than the one observed on NF for cells seeded on PLGA-GO 2%, but not on 5% (Fig. 6E). Human lung cancer cell lineage displayed a significantly higher ROS production on t3 with respect to NF, in accordance with murine breast cancer cells (Fig. 6F). However, in this case, even PLGA-GO 1% induced a strong production of ROS on cancer cells. For all samples, PLGA-GO 5% scaffolds caused a production of ROS even without NIR radiation, in accordance with the loss in viability, due to the high concentration of GO. Our experimental findings revealed that irradiated scaffolds containing 1% and 2% GO exhibited a remarkable increase in ROS production compared to the control scaffolds, resulting in a significant decrease in cancer cell viability. These observations suggest that the inclusion of GO at these concentrations enhances the oxidative stress on cancer cells, potentially leading to cell death. Conversely, scaffolds with 0.5% GO demonstrated cellular responses akin to those seen with PLGA

scaffolds alone, indicating that the presence of 0.5% GO did not significantly alter the cellular behavior compared to pure PLGA scaffolds. Scaffolds with 5% GO exhibited considerable toxicity even without NIR irradiation, particularly affecting non-cancerous cells, in accordance with findings on PBMC. The inherent toxicity observed at this GO concentration raised concerns about its potential adverse effects, moreover, the thermal effects induced by scaffolds containing 5% GO were found to be similar to those with 2% GO, suggesting that the higher GO concentration did not confer any additional advantage in terms of thermal properties. Considering these experimental results, we have excluded scaffolds with 0.5% (not effective) and 5% GO from further investigations.

These results highlight the crucial role of the presence of GO on inducing a cytotoxic effect mediated by the generation of free radicals. We observed that the concentration of GO in the 3D printed scaffolds represents a fundamental factor that must be taken into account due to the different biological effect observed on two cancer cell lines. Mouse breast cancer cells showed a higher sensitivity to scaffolds having 2% GO indeed, while lung cancer cells displayed a strong biological response even at 1% of GO. By tuning the right concentration of the photoabsorber, it is possible to achieve a selective destruction of tumor cells while minimizing damage to healthy tissues. Importantly, we observed that not only the concentration of GO, but also the selection of a proper NIR dose is crucial to modulate the production of ROS and cytotoxicity. The production of free radicals in mouse macrophages after t3 with respect to NF, along with its stronger killing effect on both tested cancer cell lineages can furtherly enhance antitumor activity via activation and stimulation of the immune system towards cancer region, possibly inducing a long-lasting and specific immunogenic response [44, 45].

3.7. Effect of NIR radiation regimens on pro-inflammatory cytokines secretion by tumor cells

To investigate how NIR regimens could affect PLGA or PLGA-GO cultured tumor cells, pro-inflammatory cytokines release was assayed in cellular supernatants after treatments. NIR treatments were conducted on mouse 4T1 and human A549 cells as described above, and interleukin 8 (IL-8), tumor necrosis factor α (TNF- α) and interleukin 6 (IL-6) production was quantified in the culture supernatants by ELISA method (Fig. 7), as picograms of cytokines produced per cellular viability. IL-8 is a chemokine involved in the innate immune responses and in the recruitment of acute inflammatory cells, such as neutrophils and other granulocytes, and TNF-α and IL-6 are secreted under cellular oxidative stress condition. We demonstrated that the presence of GO in both percentages could affect the cellular secretion of proinflammatory elements under single and repeated NIR regimens. In our human cellular model, we observed a higher content of IL-8 and TNF-α upon both NIR regimens, as compared to not irradiated groups. Furthermore, cells revealed the same capability of cytokines production when cultured on PLGA-GO 1% and 2%, highlighting the responsiveness of the scaffold. The highest level of IL-6 secretion was found to be in t3 regimen. On the other hand, NIR treatment appeared to be more efficacious on cytokines production when 4T1 cells were cultured on PLGA-GO 2%, indicating a GO-dependent effect, taking also into account the cellular viability/mortality. TNF-α seemed to be less influenced when t3 regimen was applied.

3.8. Impact of NIR radiation regimens on immune response of mouse macrophages

The RAW264.7 cells are monocyte/macrophage-like cell lineage [46, 47] well-characterized with respect to macrophage-mediated immune, metabolic, and phagocytic functions [48]. To evaluate the performance of the PTT treatment on immune response, Raw 264.7 cells was cultured in the presence of PLGA and PLGA-GO scaffolds with or without NIR

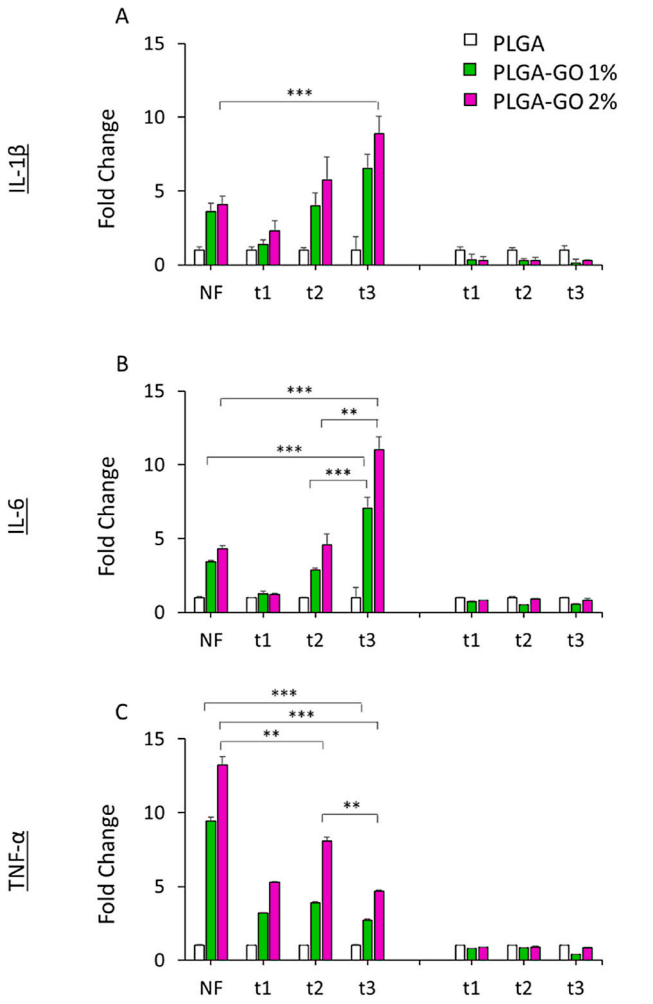

Fig. 8. Immune response of mouse macrophages. **A**) Expression of IL-1β by RAW264.7 cell line. **B**) Expression of IL-6 by RAW264.7 cell line. **C**) Expression of TNF-α by RAW264.7 cell line. Data are reported as fold change with respect to cells seeded on PLGA. **p > 0.01 and ***p > 0.001 ANOVA and Turkey post-hoc test.

laser treatment and inflammatory cytokines secretion was investigated. Fig. 8 shows the production of IL-1β, IL-6 and TNF-α 24 h s after repeated and single NIR irradiation regimens. Inflammatory cytokines secretion by mouse Raw264.7 cells was observed to be both scaffold composition-dependent and time-dependent after NIR laser treatment. A significant time-dependent effect of NIR laser treatment on cytokines secretion was observed in the presence of PLGA-GO scaffolds. A very significant increase of TNF-α by RAW-264.7 macrophages was particularly observed 24 h s after single NIR treatment in the presence of PLGA-GO 2% scaffolds compared to the same samples irradiated with repeated NIR laser irradiation. A gradual increase of TNF-α was actually observed in the RAW-264.7 cells irradiated with repeated NIR treatment (48 h s after the second treatment). Then, a significant decrease of TNF-α and concomitant increase of IL-6 were observed 72 h s after RAW-264.7 cells irradiation (t3) in the presence of PLGA/GO 2% scaffolds [49]. We observed a significant increase of IL-6 in the culture medium of RAW-264.7 macrophages treated with single NIR irradiation, that was comparable to the value measured 24 h s after RAW-264.7 cells were exposed to 3-min NIR laser (t1 time point). IL-1β secretion increased in a NIR laser dose-dependent manner following repeated laser treatment. The single dose of NIR laser irradiation (NF) triggered an effective release of IL-1β in the culture medium by RAW-264.7 macrophages in comparison with the same cells exposed to 3 min-NIR laser irradiation,

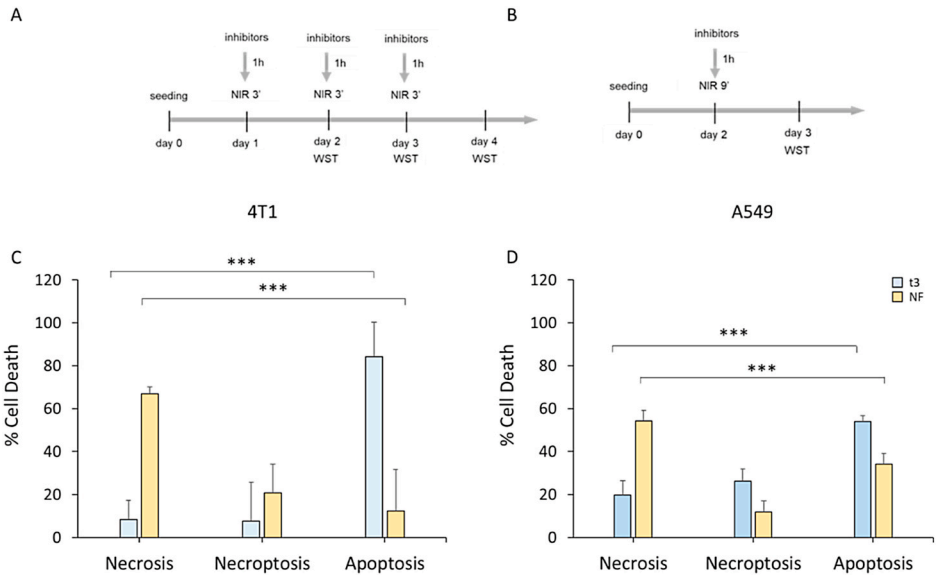

Fig. 9. Cell death induced on cancer cells after NIR treatment regimens. **A)** Schematic representation of the design of the experiments for apoptosis and necroptosis in the t3 NIR regimen. Caspase- or RIPK1-inhibitors were added three times into the wells at final concentrations of 20 μM before each NIR irradiation. **B)** Schematic representation of the design of the experiments for apoptosis and necroptosis in the NF NIR regimen. Caspase- or RIPK1-inhibitors were added once into the wells at final concentrations of 20 μM before NIR irradiation. **C**) Percentage of different types of cell death induced by NIR on mouse mammary tumor. **D**) Percentage of different types of cell death induced by NIR on mouse mammary tumor. ***$p < 0.001$ ANOVA and Turkey post-hoc test.

that released undetectable amounts of this cytokine, as measured 24 h s after laser treatment. The amount of IL-1β release, however, was smaller when compared to IL-1β amounts secreted by RAW-264.7 cells ater 72 h s post-repeated NIR laser irradiation.

3.9. Cell death pattern induced by photodynamic effects of PLGA-GO in cancer cells

PDT mediated hyperthermia can kill cells through induction of necrosis, apoptosis or through necroptosis [50,51]. We investigated whether different hyperthermia regimens could impact cell death pathway induced by means of NIR-activated PLGA-GO 2% scaffolds in cancer cell lines, we set up an in vitro assay treating first cells with specific cell death pathways inhibitors and then applying NIR laser irradiation at above indicated conditions [52]. We seeded 4T1 murine mammary carcinoma and human A549 lung carcinoma cells on PLGA-GO scaffolds in the presence of 20 μM pan-caspase inhibitor Z-VAD-FMK that blocks the induction of apoptosis or 20 μM 7-Cl-O--Nec-1 (RIP1 inhibitor II) that selectively blocks RIP1-dependent necroptosis (Fig. 9A–B) [53–55]. After NF and t3 NIR irradiation, cell viabilities were then measured using WST-1 assay and different type of cell death were discriminated by the specific pathways inhibitor. Percentage of necrotic, necroptotic and apoptotic cells after repeated and single NIR irradiation regimens are showed in Fig. 9. Repeated 3-min NIR treatment killed 4T1 mouse breast cancer cells mainly through RIP-1-independent apoptosis (84,1%), while the cell death pattern switched to necrosis-dominant when the single 9-min NIR regimen was applied. Apoptosis was the principal cell death pathway (54%) also for A549 lung cancer cells treated with repeated 3-min NIR irradiations, even though necroptosis (26%) and necrosis (19,87%) play a role in the PLGA-GO2%-induced cell death. In contrast, single 9-min irradiation resulted in 54% of necrosis in A549 cells; notably this treatment also led to a mixed cell death pattern, considering apoptosis and necroptosis percentages (34 % and 11.9 %, respectively). These data demonstrate that cell death pathways executed upon NIR irradiation in cancer cells grown on GO-based scaffolds seem to be NIR laser dose-dependent. PDT killed tumor cells mainly through apoptosis when the NIR radiation was administered in three separate days (t3). Necrosis was, conversely, the principal mechanism for PDT-induced cell death in the NF treatment regimen. A minor contribution of dose-induced necroptosis to cell death was observed in both cancer cell lines after photothermal/photodynamic treatment even though the difference between the percentages of this cell death mechanism was not statistically significant.

3.10. In vivo photo dynamic therapy

Since the in vitro experiments have demonstrated the high tumor selectivity and excellent antitumor property of scaffolds, their efficacy was investigated in vivo. Mice were inoculated subcutaneously with 4T1-Luc2 cells, expressing luciferase through lentiviral vector encoding firefly luciferase gene (luc2) under control of EF-1 alpha promoter. One week post tumor challenge, four groups were randomly established ($n = 4$): tumor (without adding any scaffolds or NIR (T), tumor and scaffold (TS), tumor, scaffold and a single NIR radiation of 9 min (NF), tumor, scaffold and 3 NIR radiations of 3 min each -one per day (t3). TS, NF and t3 groups went on subcutaneous surgical insertion of the PLGA-GO 2% scaffold beneath the tumor area. The 2% GO concentration was chosen in accordance with our in vitro findings on 4T1 cell lineage. After surgical insertion of the scaffolds, NIR radiation was carried out on mice keeping the power density fixed at 0.8 W/cm^2 as for the in vitro experiments. The two NIR radiation doses tested in vitro were administered also on tumor-bearing mice for PTT/PDT. To provide direct evidence of the photothermal/photodynamic properties of our scaffold in vivo, during NIR irradiation, thermographic images were captured using a thermal camera. A sharp rapid increase of the local tumor temperature after NIR irradiation was found when scaffolds were irradiated with NF or t3 doses while the tissue surrounding the tumor showed very little photothermal effects, reducing hyperthermia damage to the healthy tissue. T and TS groups did not show any potential temperature effects during the observation periods. (Fig. 10A). The local temperature of TS group was only around 35 °C, which is identical to the tumor temperature of T group. We evaluated the bioluminescence after intraperitoneal injection of D-luciferin using the Optical Imaging IVIS® System, by acquiring images every 7 days to monitor tumor growth. Results are shown in Fig. 10 in terms of luminescence intensity of the

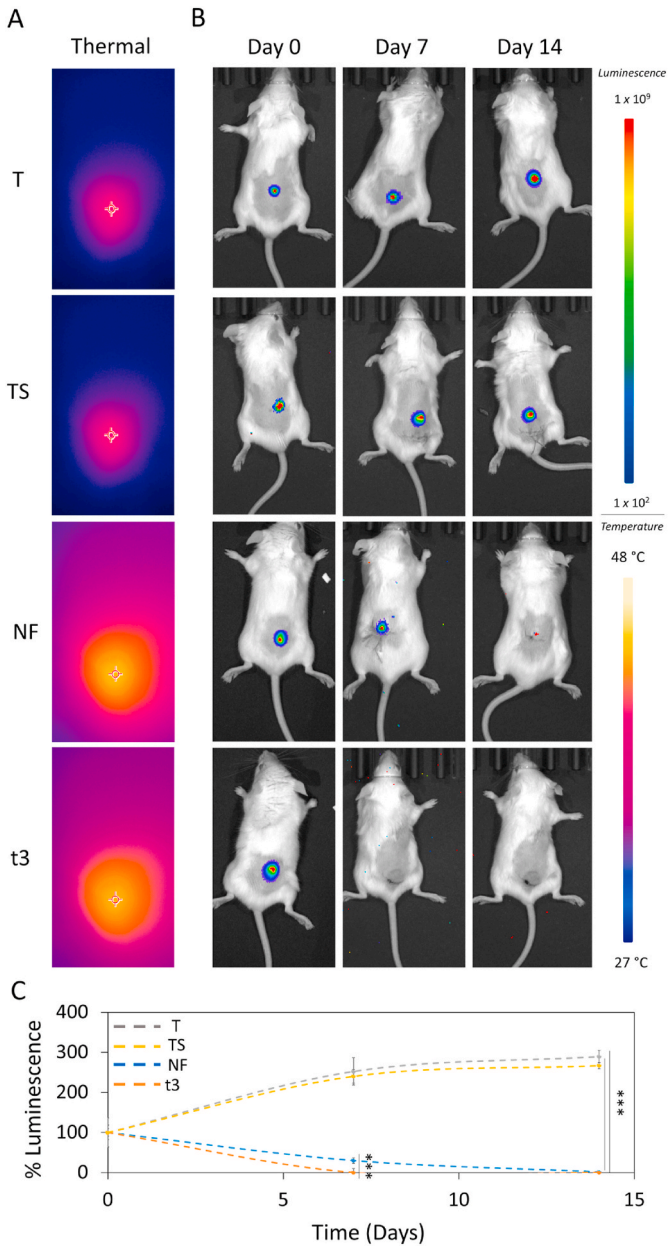

Fig. 10. In vivo NIR radiation. **A**) Images of the localized thermal increase with a thermal camera focused on cancer region in vivo. **B**) In vivo luminescence intensity on the four experimental groups (T, TS, NF and t3). **C**) Luminescence intensity over time. Luminescence was expressed as % of day 0 for each experimental group. ***$p < 0.001$ ANOVA and Turkey post-hoc test.

oxidized luciferin. After photothermal/photodynamic treatment, tumor bioluminescence in NF and t3 groups was observed to be remarkably reduced over time, where increased in T and TS groups. At the end of the 14th day no luminescence signal was observed in whole-body bioluminescent images of NF and T3 groups. However, a difference between the two therapeutic approaches was observed at day 7, as shown in the representative images of mice through IVIS® System (Fig. 10B). Mice treated with t3 showed strong reduction in bioluminescent tumor signal compared to the NF group. Luminescence intensity of luciferin was quantified and reported in Fig. 10C. Results are expressed as % luminescence intensity at 0, 7 and 14 days with respect to day 0 for each experimental group. After 7 days, NF group showed luminescence intensity reduced to 30%, with respect to its day 0, indicating a strong inhibition effect on tumor growth. Importantly, just after 7 days, we observed no luminescence signal in all mice from t3 group, indicating that this tuning of the NIR dose administration exhibited the best effect when compared to NF treatment. Both T control and TS groups displayed luminescence intensity increased up to 250% with respect to their day 0, indicating a fast tumor growth rate and proving that NIR irradiation is necessary for this scaffold to show the anticancer effect. These results agree with our experimental findings on 4T1 in vitro. After two weeks, no luminescence signal was observed for both treatments, while both T and TS showed a further increase in tumor luminescence intensity, as a further proof of the anticancer effect of our photocancer therapy. The inhibition ratios of different NIR regimens were also calculated (Figure S1). These ratios showed that the PLGA-GO 2% scaffold under T3 NIR Irradiation regimen performed strongest inhibition to the tumor growth with a final ratio over 99% after 7 days treatment, confirming its high efficiency for tumor therapy.

3.11. Histological analysis

The tissue was examined histologically to evaluate the photothermal and photodynamic effect obtained by NIR irradiation (Fig. 11). Tumor histology in the T and TS groups exhibited high-grade carcinoma without significant lymphomonocytic infiltrate (Fig. 11A and B), wherein tissue analysis showed healthy skin without neoplasia in hematoxylin and eosin (H&E) stained images of NF and t3 groups (Fig. 11C and D). To determine whether PLGA or PLGA-GO 2% scaffold induce inflammatory response, at the end of the experiments, we evaluated the systemic release of key proinflammatory biomarkers. As shown in Figure S2, the serum levels of TNF-α and IL-6 were under the detection threshold in each group, indicating that the inflammatory response was not induced by in vivo exposure to scaffolds. MIP- 2, a chemokine involved in the recruitment of acute inflammatory cells, was constitutively expressed at very low levels, showing no difference among the experimental groups. The body weight of all groups further revealed no significant difference, confirming that no obvious toxicity was induced by either PLGA or PLGA-GO 2% scaffolds (Figure S3). These results suggest that PLGA-GO 2% scaffold or + NIR irradiation significantly inhibited tumor growth and displayed excellent photothermal therapy ability in vivo.

3.12. In vivo photo dynamic therapy for non-direct contact tumors

To investigate the effect of NIR therapy on noncontact tumors, 4T1 cells were subcutaneously injected into tumor-bearing mice to establish a recurrent tumor model. In order to comprehensively assess the efficacy of our proposed fractionated photodynamic therapy, we conducted in vivo experiments utilizing a tumor site in proximity to the scaffold but not in direct contact with it. This deliberate choice aimed to simulate the clinical scenario of recurrent tumors that may reoccur in the same original treatment site but not in direct contact with the scaffold. One week after injection, scaffolds were implanted under the primary tumor and NIR radiation was performed. For this purpose, we focused on the therapeutic protocol that resulted in the highest antitumor efficiency, the fractionated dose t3. As for the previous experiment, we monitored the bioluminescence intensity after intraperitoneal injection of D-luciferin using the Optical Imaging IVIS® System, by acquiring images every 7 days (Fig. 12A). Results of % luminescence are shown in Fig. 12B. Both in direct contact (T I) and not in direct contact (T II) tumors depicted a significant growth of 272 ± 15 % and 215 ± 12 % respectively when compared to their day 0 in control group. Importantly, based on our evidence, both the treated in contact (t3 I) and the not in direct contact tumor (t3 II) of t3 showed a strongly significant reduction in tumor growth in terms of % luminescence. These findings furtherly verified the high antitumor effect of t3 NIR not only against primary tumor, but also against the not directly treated tumor, holding a great potential in the application of targeting cancer with no adverse effects.

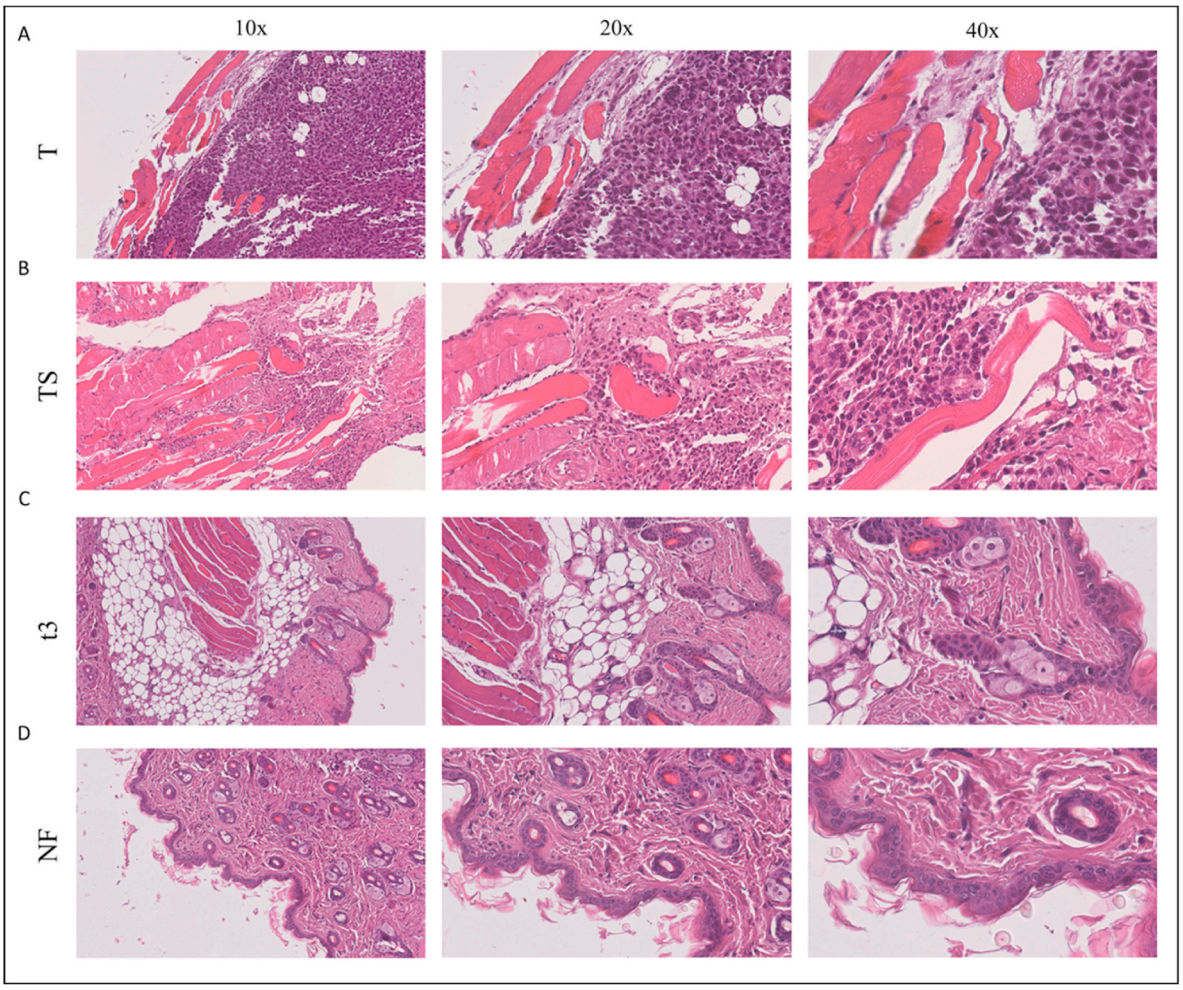

Fig. 11. Histological images of tissue samples from mice at 10×, 20× and 40× magnification. **A**) **A** Representative image of a T sample after the experimental timespan. **B**) Representative image of a TS sample after the experimental timespan. **C**) Representative image of a t3 sample after NIR radiation, showing healthy skin. **D**) Representative image of a NF sample after NIR radiation, showing healthy skin.

4. Conclusions

In this study, we report remarkable advancements in the field of biomaterials and tissue engineering, showcasing the use of 3D printing technology of PLGA-GO to create a potent therapeutic platform. The unique attributes of GO, including its biocompatibility, drug-loading capacity, and photothermal/photodynamic characteristics, position it as an ideal candidate for multifunctional therapeutics in cancer treatment. Importantly, this work marks the first attempt to optimize NIR radiation protocols for anticancer therapy. Our investigation focused on comparing two distinct photothermal/photodynamic therapeutic strategies – a single radiation session (NF) and a fractionated approach over three consecutive days (t1, t2, and t3) – utilizing innovative 3D printed GO-PLGA scaffolds. The comprehensive assessment encompassed both in vitro and in vivo evaluations, providing critical insights into the comparative efficacy of these strategies. Notably, in our in vitro experiments, we observed significant differences in response to the two different NIR doses. Cancer cells subjected to the single radiation session (NF) exhibited a shift in their death mechanisms towards necrosis. On the other hand, cancer cells treated with the fractionated dose (t3) displayed a different type of cell death, characterized by a shift towards apoptosis. In both in vitro and in vivo settings, the fractionated approach (t3) exhibited heightened efficacy in the eradication of cancer cells, thereby emphasizing its potential as a robust and precisely targeted strategy for anticancer intervention. Furthermore, our findings highlighted the immense potential of NIR-mediated PTT/PDT in achieving targeted cancer cell eradication, enhancing immune polarization and stimulation The comprehensive evaluation of different doses of NIR radiation emphasizes the importance of optimizing and standardizing PTT/PDT protocols to maximize therapeutic benefits. This pioneering work adds to the mounting evidence supporting the clinical translation of NIR-based therapeutic approaches and underscores the need for further research to fully harness their potential in cancer therapy. In the context of surgical reconstruction after oncologic procedures, the incorporation of nanomaterials like graphene into scaffolds introduces an innovative dimension to cancer therapy. These scaffolds, tailored to specific anatomical sites, serve as strategic platforms for the localized delivery of PTT/PDT. Placing photosensitizing nanomaterials within these scaffolds enables targeted local treatments precisely where the risk of tumor recurrence is highest. This groundbreaking approach addresses a critical challenge in cancer therapy—the prevention of local recurrence following surgical interventions. By combining the precision of PTT/PDT with the unique properties of advanced nanomaterials, we open avenues for highly localized and effective treatments. In conclusion, our study not only emphasizes the effectiveness of 3D printed GO-PLGA scaffolds in cancer treatment but also unveils significant differences in response to the two distinct NIR doses both in vitro and in vivo. Our findings open avenues for the development of more potent and targeted therapies within the emerging field of PTT/PDT-based treatments.

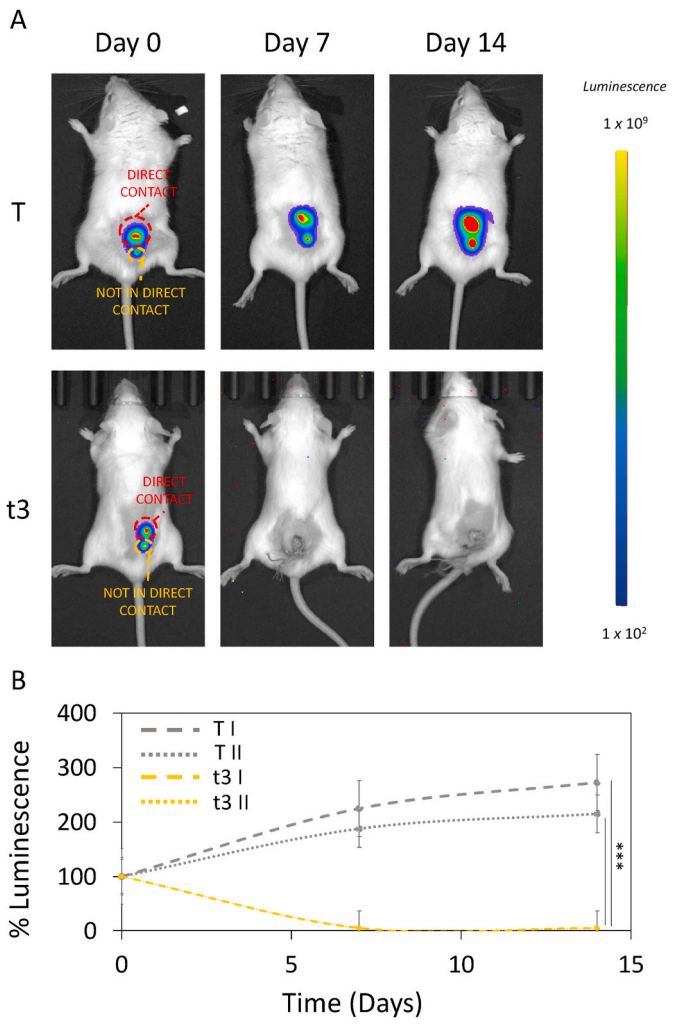

Fig. 12. In vivo NIR radiation against not in direct contact tumor. **A)** In vivo luminescence intensity on the two experimental groups, having an in direct contact and a not in direct contact tumor (T I, T II, t3 I and t3 II). **B)** Luminescence intensity over time. Luminescence was expressed as % of day 0 for each experimental group. ***p < 0.001 ANOVA and Turkey post-hoc test.

CRediT authorship contribution statement

Giordano Perini: Writing – original draft, Validation, Investigation, Formal analysis, Data curation. **Valentina Palmieri:** Visualization, Methodology, Investigation, Data curation. **Andrea Papait:** Writing – original draft, Formal analysis, Data curation. **Alberto Augello:** Methodology, Investigation, Formal analysis. **Daniela Fioretti:** Investigation, Formal analysis, Data curation. **Sandra Iurescia:** Investigation, Formal analysis, Data curation. **Monica Rinaldi:** Investigation, Formal analysis. **Elsa Vertua:** Formal analysis, Data curation. **Antonietta Silini:** Funding acquisition, Formal analysis. **Riccardo Torelli:** Methodology, Investigation, Formal analysis. **Angela Carlino:** Formal analysis, Data curation. **Teresa Musarra:** Formal analysis, Data curation. **Maurizio Sanguinetti:** Methodology, Investigation. **Ornella Parolini:** Methodology, Investigation, Formal analysis, Data curation. **Marco De Spirito:** Writing – review & editing, Validation, Methodology. **Massimiliano Papi:** Writing – review & editing, Supervision, Resources, Project administration, Methodology, Investigation, Funding acquisition, Data curation, Conceptualization.

Declaration of competing interest

The authors declare that they have no known competing financial interests or personal relationships that could have appeared to influence the work reported in this paper.

Data availability

Data will be made available on request.

Acknowledgements

The research leading to these results has received funding from AIRC under IG 2019—ID. 23124 project—P.I. Massimiliano Papi.

We would like to acknowledge the contribution of 3D Bioprinting Research Core Facility G-STeP and Microscopy Core Facility G-STeP of the Fondazione Policlinico Universitario "A. Gemelli" IRCCS for sample processing.

Appendix A. Supplementary data

Supplementary data to this article can be found online at https://doi.org/10.1016/j.mtbio.2024.100986.

References

[1] A.S. Sogomonyan, et al., 3D models of cellular spheroids as a universal tool for studying the cytotoxic properties of anticancer compounds in vitro, Acta Naturae 14 (2022) 92.
[2] J.O. Winter, S.S. Rao, Tissue Engineering Models for Cancer Pathology, 2022.
[3] A. Do, B. Khorsand, S.M. Geary, A.K. Salem, 3D printing of scaffolds for tissue regeneration applications, Adv. Healthcare Mater. 4 (2015) 1742–1762.
[4] F. Causa, P.A. Netti, L. Ambrosio, A multi-functional scaffold for tissue regeneration: the need to engineer a tissue analogue, Biomaterials 28 (2007) 5093–5099.
[5] G. Lutzweiler, A. Ndreu Halili, N. Engin Vrana, The overview of porous, bioactive scaffolds as instructive biomaterials for tissue regeneration and their clinical translation, Pharmaceutics 12 (2020) 602.
[6] N.Z. Laird, et al., Applications of nanotechnology in 3D printed tissue engineering scaffolds, Eur. J. Pharm. Biopharm. 161 (2021) 15–28.
[7] A. Zaszczyńska, B. Niemczyk-Soczynska, P. Sajkiewicz, A comprehensive review of electrospun fibers, 3D-printed scaffolds, and hydrogels for cancer therapies, Polymers 14 (2022) 5278.
[8] H. Bhuskute, P. Shende, B. Prabhakar, 3D printed personalized medicine for cancer: applications for betterment of diagnosis, prognosis and treatment, AAPS PharmSciTech 23 (2022) 1–12.
[9] V. Palmieri, et al., 3D-printed graphene for bone reconstruction, 2D Mater. 7 (2020) 22004.
[10] V. Palmieri, G. Perini, M. De Spirito, M. Papi, Graphene oxide touches blood:: in vivo interactions of bio-coronated 2D materials, Nanoscale Horiz. 4 (2019) 464–471.
[11] K. Krishnamoorthy, M. Veerapandian, K. Yun, S.J. Kim, The chemical and structural analysis of graphene oxide with different degrees of oxidation, Carbon N Y 53 (2013) 38–49.
[12] V. Palmieri, M. Papi, Can graphene take part in the fight against COVID-19? Nano Today (2020) 100883.
[13] A.G. Marrani, et al., A comparative experimental and theoretical study of the mechanism of graphene oxide mild reduction by ascorbic acid and N-acetyl cysteine for biomedical applications, Mater. Adv. 1 (2020) 2745–2754.
[14] F. De Maio, et al., 3D-printed graphene polylactic acid devices resistant to SARS-CoV-2: sunlight-mediated sterilization of additive manufactured objects, Carbon N Y 194 (2022) 34–41.
[15] G. Perini, V. Palmieri, G. Ciasca, M. De Spirito, M. Papi, Unravelling the potential of graphene quantum dots in biomedicine and neuroscience, Int. J. Mol. Sci. 21 (2020) 3712.
[16] V. Palmieri, et al., Graphene oxide-mediated copper reduction allows comparative evaluation of oxygenated reactive residues exposure on the materials surface in a simple one-step method, Appl. Surf. Sci. 615 (2023) 156315.
[17] T. Dutta, et al., ROS generation by reduced graphene oxide (rGO) induced by visible light showing antibacterial activity: comparison with graphene oxide (GO), RSC Adv. 5 (2015) 80192–80195.
[18] L. Jacquemin, et al., Mechanisms of radical formation on chemically modified graphene oxide under near infrared irradiation, Small 19 (2023) 2207229.
[19] Y. He, A. Del Valle, Y. Qian, Y.-F. Huang, Near infrared light-mediated enhancement of reactive oxygen species generation through electron transfer from graphene oxide to iron hydroxide/oxide, Nanoscale 9 (2017) 1559–1566.
[20] G. Perini, et al., Carboxylated graphene quantum dots-mediated photothermal therapy enhances drug-membrane permeability, ROS production, and the immune system recruitment on 3D glioblastoma models, Cancer Nanotechnol. 14 (2023) 13.
[21] F. Sun, et al., Application of 3D-printed, PLGA-based scaffolds in bone tissue engineering, Int. J. Mol. Sci. 23 (2022) 5831.

[22] L. Sutrisno, et al., PLGA–collagen–BPNS bifunctional composite mesh for photothermal therapy of melanoma and skin tissue engineering, J. Mater. Chem. B 10 (2022) 204–213.
[23] C.V. Rocha, V. Gonçalves, M.C. da Silva, M. Bañobre-López, J. Gallo, PLGA-based composites for various biomedical applications, Int. J. Mol. Sci. 23 (2022) 2034.
[24] L. Leung, C. Chan, S. Baek, H. Naguib, Comparison of morphology and mechanical properties of PLGA bioscaffolds, Biomed. Mater. 3 (2008) 025006.
[25] A.N.F. Versypt, D.W. Pack, R.D. Braatz, Mathematical modeling of drug delivery from autocatalytically degradable PLGA microspheres—a review, J. Contr. Release 165 (2013) 29–37.
[26] G. Perini, et al., Graphene quantum dots' surface chemistry modulates the sensitivity of glioblastoma cells to chemotherapeutics, Int. J. Mol. Sci. 21 (2020) 6301.
[27] G. Perini, et al., Inhibiting the growth of 3D brain cancer models with bio-coronated liposomal temozolomide, Pharmaceutics 13 (2021), https://doi.org/10.3390/pharmaceutics13030378. Preprint at.
[28] G. Perini, et al., Functionalized Graphene Quantum Dots Modulate Malignancy of Glioblastoma Multiforme by Downregulating Neurospheres Formation. *C*, vol. 7, 2021, https://doi.org/10.3390/c7010004. Preprint at.
[29] V. Palmieri, et al., Biocompatible: N -acetyl cysteine reduces graphene oxide and persists at the surface as a green radical scavenger, Chem. Commun. 55 (2019) 4186–4189.
[30] G. Perini, et al., Advanced usage of Ti3C2Tx MXenes for photothermal therapy on different 3D breast cancer models, Biomed. Pharmacother. 153 (2022) 113496.
[31] A. Rosenkranz, et al., Laser-mediated antibacterial effects of few- and multi-layer Ti3C2Tx MXenes, Appl. Surf. Sci. 567 (2021) 150795.
[32] M.B. Ericson, A.-M. Wennberg, O. Larkö, Review of photodynamic therapy in actinic keratosis and basal cell carcinoma, Therapeut. Clin. Risk Manag. 4 (2008) 1–9.
[33] J. Usuda, et al., Photodynamic therapy (PDT) for lung cancers, J. Thorac. Oncol. 1 (2006) 489–493.
[34] T. Kubrak, M. Karakuła, M. Czop, A. Kawczyk-Krupka, D. Aebisher, Advances in management of bladder cancer—the role of photodynamic therapy, Molecules 27 (2022).
[35] P. Sekhri, D.K. Ledezma, A. Shukla, E.E. Sweeney, R. Fernandes, The thermal dose of photothermal therapy generates differential immunogenicity in human neuroblastoma cells, Cancers 14 (2022) 1447.
[36] M. Overchuk, R.A. Weersink, B.C. Wilson, G. Zheng, Photodynamic and photothermal therapies: synergy opportunities for nanomedicine, ACS Nano 17 (2023) 7979–8003.
[37] A.R. Silini, et al., CM from intact hAM: an easily obtained product with relevant implications for translation in regenerative medicine, Stem Cell Res. Ther. 12 (2021) 540.
[38] T. Arasoglu, S. Derman, B. Mansuroglu, Comparative evaluation of antibacterial activity of caffeic acid phenethyl ester and PLGA nanoparticle formulation by different methods, Nanotechnology 27 (2016) 25103.
[39] D. Edith, J.-L. Six, Surface characteristics of PLA and PLGA films, Appl. Surf. Sci. 253 (2006) 2758–2764.
[40] S. Chaiyakun, et al., Preparation and characterization of graphene oxide nanosheets, Procedia Eng. 32 (2012) 759–764.
[41] A.G. Marrani, R. Zanoni, R. Schrebler, E.A. Dalchiele, Toward graphene/silicon interface via controlled electrochemical reduction of graphene oxide, J. Phys. Chem. C 121 (2017) 5675–5683.
[42] C.-H. Lee, C.-H. Hong, W.-T. Liao, H.-S. Yu, Differential immunological effects of infrared irradiation and its associated heat in vivo, J. Photochem. Photobiol., B 155 (2016) 98–103.
[43] W.-T. Liao, et al., Anti-Inflammatory effects induced by near-infrared light irradiation through M2 macrophage polarization, J. Invest. Dermatol. 141 (2021) 2056–2066.
[44] P. Xu, F. Liang, Nanomaterial-based tumor photothermal immunotherapy, Int. J. Nanomed. 15 (2020) 9159.
[45] C. Xu, Y. Jiang, Y. Han, K. Pu, R. Zhang, A polymer multicellular nanoengager for synergistic NIR-II photothermal immunotherapy, Adv. Mater. 33 (2021) 2008061.
[46] R.L. Randall, A promise to our patients with metastatic bone disease, Ann. Surg Oncol. 21 (2014) 4049–4050.
[47] G. Gravis, Systemic treatment for metastatic prostate cancer, Asian J. Urol. 6 (2019) 162–168.
[48] J.W. Hartley, et al., Expression of infectious murine leukemia viruses by RAW264.7 cells, a potential complication for studies with a widely used mouse macrophage cell line, Retrovirology 5 (2008) 1–6.
[49] L.E. DeForge, D.G. Remick, Kinetics of TNF, IL-6, and IL-8 gene expression in LPS-stimulated human whole blood, Biochem. Biophys. Res. Commun. 174 (1991) 18–24.
[50] M. Pérez-Hernández, et al., Dissecting the molecular mechanism of apoptosis during photothermal therapy using gold nanoprisms, ACS Nano 9 (2015) 52–61.
[51] Y. Zhang, et al., Temperature-dependent cell death patterns induced by functionalized gold nanoparticle photothermal therapy in melanoma cells, Sci. Rep. 8 (2018) 8720.
[52] M. Kim, et al., Numerical study on effective conditions for the induction of apoptotic temperatures for various tumor aspect ratios using a single continuous-wave laser in photothermal therapy using gold nanorods, Cancers 11 (2019), https://doi.org/10.3390/cancers11060764. Preprint at.
[53] C.J.F. Van Noorden, The history of Z-VAD-FMK, a tool for understanding the significance of caspase inhibition, Acta Histochem. 103 (2001) 241–251. Preprint at.
[54] S.H. Needs, M.D. Bootman, J.E. Grotzke, H.B. Kramer, S.A. Allman, Off-target inhibition of NGLY1 by the polycaspase inhibitor Z-VAD-fmk induces cellular autophagy, FEBS J. 289 (2022) 3115–3131.
[55] H. Ushijima, R. Monzaki, An in vitro evaluation of the antioxidant activities of necroptosis and apoptosis inhibitors: the potential of necrostatin-1 and necrostatin-1i to have radical scavenging activities, Pharmacol. Rep. 75 (2023) 490–497.